OPTICAL CHARACTERIZATION OF SILICON BASED HYDROGENATED AMORPHOUS THIN FILMS BY UV-VISIBLE AND INFRARED MEASUREMENTS

A THESIS SUBMITTED TO
THE GRADUATE SCHOOL OF NATURAL AND APPLIED SCIENCES
OF
MIDDLE EAST TECHNICAL UNIVERSITY

BY

İLKER KILIÇ

IN PARTIAL FULFILLMENT OF THE REQUIREMENTS

FOR

THE DEGREE OF MASTER OF SCIENCE

IN

PHYSICS

JANUARY 2006

Approval of the Graduate School of Natural and Applied Sciences.

Prof. Dr. Canan Özgen
Director

I certify that this thesis satisfies all the requirements as a thesis for the degree of Master of Science.

Prof. Dr. Sinan Bilikmen
Head of Department

This is to certify that we have read this thesis and that in our opinion it is fully adequate, in scope and quality, as a thesis for the degree of Master of Science.

Prof. Dr. Bayram Katırcıoğlu
Supervisor

Examining Committee Members

Assoc. Prof. Dr. Hatice Kökten (METU, PHYS) _____

Prof. Dr. Bayram Katırcıoğlu (METU, PHYS) _____

Assoc. Prof. Dr. İsmail Atılgan (METU, PHYS) _____

Assist. Prof. Dr. Hüseyin Sarı (Ank. Unv., PHYS ENG) _____

Assist. Prof. Dr. Barış Akaoğlu (Gazi Unv., PHYS) _____

I hereby declare that all information in this document has been obtained and presented in accordance with academic rules and ethical conduct. I also declare that, as required by these rules and conduct, I have fully cited and referenced all material and results that are not original to this work.

Name, Lastname: İlker Kılıç

Signature :

ABSTRACT

OPTICAL CHARACTERIZATION OF SILICON BASED HYDROGENATED AMORPHOUS THIN FILMS BY UV-VISIBLE AND INFRARED MEASUREMENTS

KILIÇ, İlker
Ms., Department of Physics
Supervisor: Prof. Dr. Bayram Katırcıoğlu

January 2006, 101 pages.

Various carbon content hydrogenated amorphous silicon carbide (a-$Si_{1-x}C_x$:H) and hydrogenated amorphous silicon (a-Si:H) thin films have been deposited on various substrates by using plasma enhanced chemical vapour deposition (PECVD) technique. Transmission spectra of these films have been determined within UV-Visible region and the obtained data were analysed to find related physical constants such as; refractive indices, thicknesses, etc. Fourier transform infrared (FT-IR) spectrometry technique has been used to determine transmission & reflection type spectra of these films. Obtained data were analysed to determine bond structures of the films. Effects of relative concentration of ethylene (C_2H_4) gas on thin film bond structure and on optical constants have been questioned.

Keywords: Transmittance, Reflectance, FT-IR, UV, Visible, Refractive Index, Absorption Coefficient, Thin Film, Optical Characterization

ÖZ

SİLİKON TABANLI HİDROJENLENMİŞ AMORF İNCE FİLMLERİN MOR ÖTESİ-GÖRÜNÜR VE KIZILÖTESİ ÖLÇÜMLER İLE OPTİK KARAKTERİZASYONU

KILIÇ, İlker
Yüksek Lisans , Fizik Bölümü
Tez Yöneticisi: Prof. Dr. Bayram Katırcıoğlu

Ocak 2006, 101 sayfa.

Çeşitli karbon içerikli hidrojenlenmiş amorf silisyum (a-$Si_{1-x}C_x$:H) ve hidrojenlenmiş amorf silisyum ince filmler (a-Si:H), plazmayla hızlandırılmış kimyasal buhar biriktirme (PECVD) yöntemiyle çeşitli tabanlar üzerine biriktirilmiştir. Bu filmlerin geçirgenlik tayfları mor ötesi-görünür bölgede ölçülerek belirlenmiş ve elde edilen veriler (kırılma indisi, kalınlık, vs.), ilgili fiziksel sabitleri bulmak için analiz edilmişlerdir. Bu filmlerin kızılötesi tayflarını belirlemek için fourier dönüşümlü kızılötesi (FT-IR) spektrometre yöntemi kullanılmıştır. Bu şekilde elde edilen veriler filimlerin bağ yapılarının belirlenmesinde kullanılmıştır. Etilen (C_2H_4) gazının göreceli konsantrasyonunun ince film bağ yapısına ve optik sabitlere
etkileri sorgulanmıştır.

Anahtar Sözcükler: Geçirme, Yansıma, FT-IR, Mor Ötesi, Görünür Bölge, Kırılma İndisi, Soğrulma Katsayısı, İnce Film, Optik Karakterizasyon.

ACKNOWLEDGMENTS

I would like to express my gratitude to my supervisor Prof. Dr. Bayram Katırcıoğlu for his guidance and support during this work.

I would like to thank Assoc. Prof. Dr. İsmail Atılgan for preparation of samples and his valuable suggestions.

I would like to acknowledge my colleague Kıvanç Sel for his assistance in FT-IR analysis, and Assist. Prof. Dr. Barış Akaoğlu for his help in UV-Visible analysis.

I would also like to thank to my friends Yücel Cengiz Özer, Esen Salçın, Selçuk Yerci, Yetkin Arslan, Mesut Taştan, Fatma Ekiz for their help, friendness and support.

Finally, I would like to express my deepest appreciation to Prof. Dr. Sinan Bilikmen.

TABLE OF CONTENTS

LIST OF TABLES

LIST OF FIGURES

CHAPTER 1

INTRODUCTION

In today‘s world, information systems are built by rather two complementary constituents [1]; electronic processors (microelectronics) and input/output devices (large area electronics). Although the first group of devices is continuously developing with unbelievable miniaturization on the crystalline silicon chip, the second class has ta stay large as a necessity of man/machine interface such as document scanners, electronic displays, printers etc. The crystalline silicon could not satisfy the requirements of these large area opto-electronic devices due to both its poor optical properties and limited dimensions. The solutions developed on the semiconductors other than the crystalline silicon have created mismatching problems with the existing silicon based microelectronic technologies.

Hydrogenated amorphous silicon (a-Si:H) seems to be a solution to the large area problem of crystalline silicon because it can be deposited at low temperatures (<300°) by the glow discharge method at reasonable cost as large area thin films on low cost substrate (such as glass and ordinary rude organic materials)[2]

Drawbacks of crystalline silicon (c-Si), (namely poor optical properties and limited geometrical area or too high cost of material), are tried to be solved nowadays by a-Si:H films.

Amorphous silicon, whose huge amount of dangling bond states around midgap energy region (10^{20} $cm^{-1}eV^{-1}$) are reduced to minute amount (10^{15} $cm^{-1}eV^{-1}$) by the hydrogen compensation process, becomes able to be selectively doped both n and p types leading to a large number of practically useful devices such as p-n, p-i-n, Schottky diodes etc. [3].

Besides, the control of the electrical conductivity over 10 orders of magnitude [4] due to its dopability, the field effect allows the sheet conductance of a-Si:H layer to be switched over 6 orders of magnitude [5]. As a result, the development of thin film transistors for addressing circuits on large area electronics is facilitated by the fact that the gate dielectric layer (mostly a-SiN_x:H film), the channel layer of a-Si:H film and the ohmic source and drain n^+-contact layers can all be deposited in the same plasma reactor (PECVD) [6].

In addition to the above outlined electronic behaviour of a-Si:H material, its optical properties are substantially improved compared with the ones of crystalline silicon. Contrary to the optical weakness of crystalline silicon (c-Si), the optical gap of a-Si:H is widened up to the visible region (~ 1.75 eV) leading to the photoconductivity spectrum, shifted to shorter light wavelength compared with crystalline silicon. In other words, the a-Si:H spectrum coincides better with the sensitivity range of human eye (the alloying ability of a-Si:H with Ge, Sn, C, N and O creates a flexibility of adjusting the optical gap from IR to UV). Moreover, the optical absorption of a-Si:H in the visible range is greater by about a factor of 20 than in the case of crystalline silicon [7, 8]. (This increase in optical absorption is a consequence of the irrelevance of the selection rules for optical transitions in

amorphous semiconductors (non-conservation of k-vector)) [9]. Thus, a thin film of only 1 m thickness absorbs most of the visible light, facilitating the fabrication of high efficiency photosensors.)

Consequently, amorphous silicon and its alloys are building stone of today‘s large area optoelectronics in the relevant market [10].

At present, there is an increasing need for a accurate knowledge of the optical constants of thin absorbing films over a wide range. Since the optical constants of the materials are not well known or determined only in a narrow wavelength range. Optical constants may be determined by a large variety of techniques which basically fall into two categories [11, 12]; photometry and ellipsometry. In photometry, film is illuminated by unpolarized radiation and the intensities of reflected or transmitted beams are measured as a function of wavelength. In ellipsometry, polarized radiation is used and both intensity and phase of the reflected or transmitted beam is determined. In general, the first category, the photometric method is chosen for the determination of optical constants because of the wider availability of the necessary instrumentation.

The main aim of this work is; to familiarize with optical characterization methods used to find the related physical parameters of thin films (applicable within UV-Visible range), and to understand thin film structure by fourier transform infrared (FT-IR) spectroscopy.

In the first part of this work, Chapter 2, basic instruments that were used to produce and analyse hydrogenated amorphous silicon carbide (a-$Si_{1-x}C_x$:H) films are explained without referring to technical details.

In Chapter 3, the expressions for the optical reflection (R) and transmittance (T) of an absorbing thin film on a transparent substrate are derived starting from related Maxwell equations. This chapter includes the basic tools that will be used to find the physical parameters of thin films and the theoretical essentials derived will be used in analysis chapter, Chapter 5.

In Chapter 4, preparation of thin films are explained in two steps without referring to details.

Chapter 5 is prepared intentionally in a pedagogical way , so that the steps of UV-Vis analysis is comprehensible by anyone reading this text, who is not professionally involved in the subject matter.

In addition to UV-Visible analysis of the samples, infrared analysis are also included in Chapter 6.

CHAPTER 2

INSTRUMENTATION

2.1 PECVD SYSTEM

PECVD System (Plasma Enhanced Chemical Vapor Deposition) is a technique that is based on the decomposition of a gaseous compound near a substrate surface (similar to chemical vapor deposition CVD). One of the reaction products is a solid layer which precipitates onto the surface such that a new conducting or insulating layer is formed. The distinction between CVD and PECVD is expressed by the different process temperatures and therefore the different qualities of the produced silicon layers. Lower deposition temperatures ($< 250°C$) along with higher deposition rates can be achieved by PECVD.

As one can infer from the above description a plasma medium should be generated in PECVD (glow discharge) system. This medium is generated by supplying energy to (by applying an electric field to) neutral gas molecules, causing the formation of charge carriers, ions and free radicals [1] between two facing parallel electrodes [34]. (See Figure 2.1) Because of greater mobility of electrons over ions, positively charged ion sheaths occur which are characterized by very low electron densities and appear as dark areas adjacent to surfaces of the electrode

[1] free radicals: atoms or group of atoms which are electrically neutral and in state of incomplete chemical bonding which makes them very reactive.

in contact with the plasma. Ions accelerated across these sheaths are known as bombarding ions due to their high energy and plays an important role in reactive etching. [33]

Among various deposition techniques, PECVD (glow discharge) is the most common method to deposit a-Si and its alloys (such as a-SiC_x:H and a-SiN_x:H). Pure amorphous silicon a-Si is actually useless for electronics, since it shows a very high density of deep defects (dangling bonds) from where trapped charge carriers easily recombine. The material properties of amorphous hydrogenated silicon a-Si:H (i.e. saturated by hydrogen) are significantly better in use for electronics, because the hydrogen atoms in a-Si:H prevent the formation of dangling bonds, so the midgap defect density is decreased. This method also serves to deposit silicon oxide (SiO_x), silicon oxide nitride (SiO_xN_x), and diamond for integrated optical wave guides. Now let‘s have a closer look at the PECVD system before explaining the reaction mechanism inside it. A typical system consists of (See Figure 2.2)

1. a source of power for the discharge (a radio frequency generator in our case)
2. a gas inlet arrangement
3. a deposition chamber (or a plasma reactor) that holds the pair of electrodes
4. a substrate heating assembly
5. a pumping system

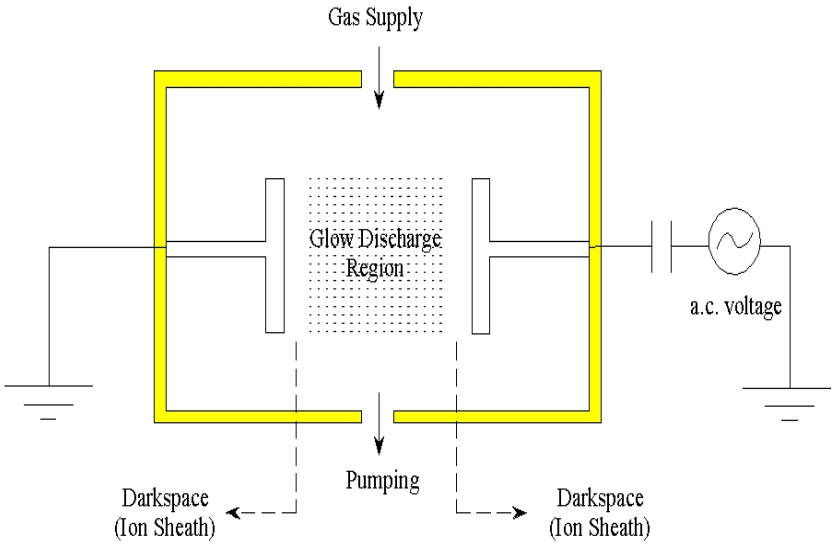

Figure 2.1: Capacitively coupled radio frequency discharge.

2.1.1 Power Source

The power is one of the main parameters that must be under an effective control. In practice, ac and dc voltages are both applied across a plasma reactor. Since a dc discharge current can not be sustained, ac current is required. ac voltages at radio frequency (RF) discharges are usually exploited when the layer to be treated is a semi-conductor or an insulator [15]. For initiation of the plasma RF power with a certain amplitude, large enough to cause the breakdown of process gas is applied to the reactor [33]. The frequency of this alternating voltage must be so high that the charged particles created in one half of the RF cycle are not fast when the current goes to zero. So the frequency range needed is typically between 50 KHz - 15 MHz. (usually 13.56 MHz) The power is applied to the top electrode in our configuration.

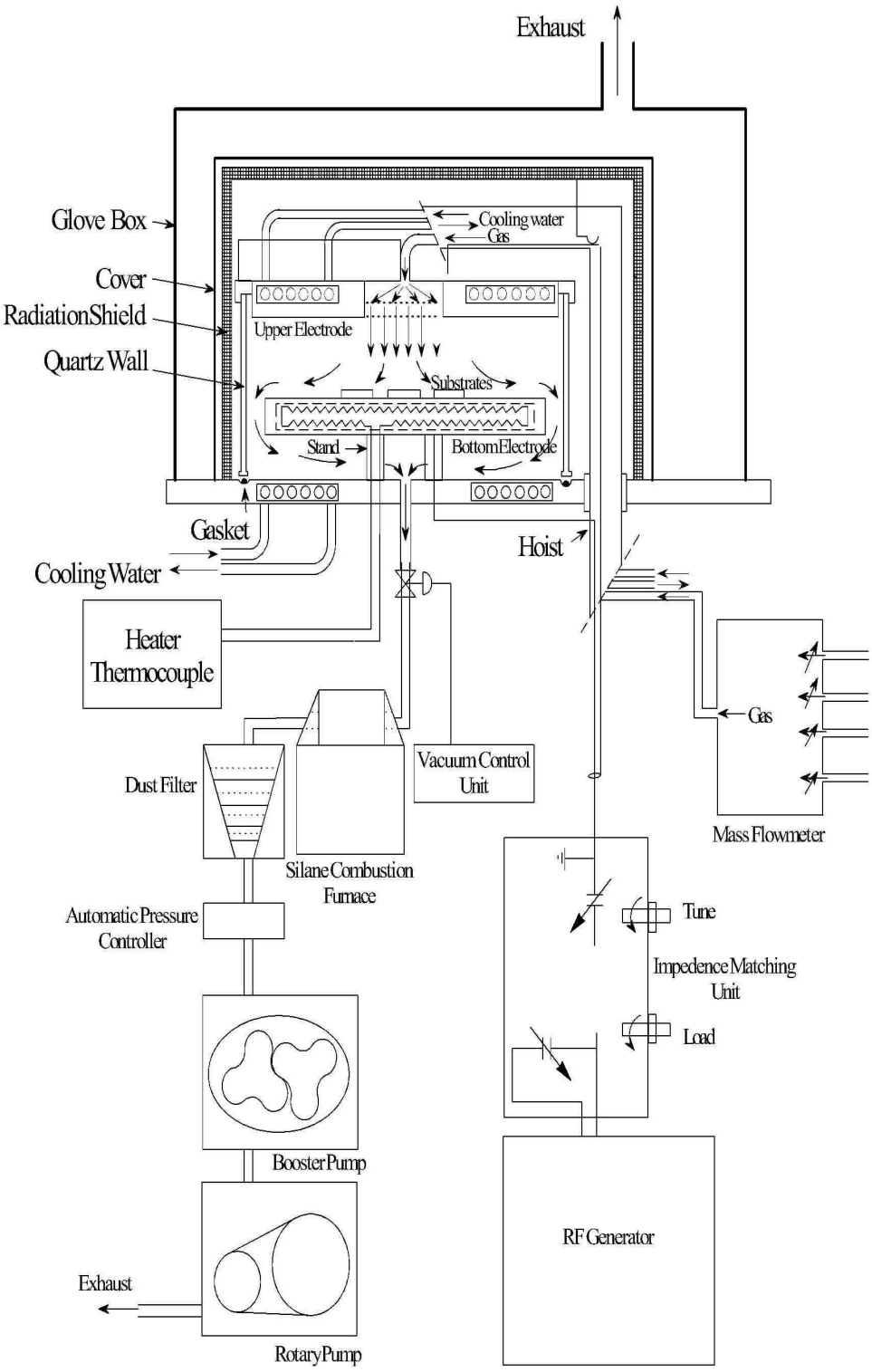

Figure 2.2: Schematic illustration of the PECVD reactor.

2.1.2 Gas Inlet Arrangement

Since gas flow process is important, gas inlet arrangement is expected to have an elaborate gas control system. It does so. This system consists of a gas cabinet (See Figure 2.3), a gas pod and a flow-meter.

The gases processed in this unit may be reactive and non-reactive. Non-reactive gases are used for purging the system where process gases are delivered. Reactive gases such as silane (SiH_4) should be placed in a cabinet which is donated with an exhaust to maintain air flow essential to eliminate any accumulation of process gases within the cabinet. This is due to the fact that, these gases are highly explosive and poisonous. Therefore most of the plumbing and connections are made of stainless steel as a precaution for gas leaks that might probably occur under pressure. Additionally stainless steel regulators, check valves, and cross purge assemblies have been utilized for safety reasons and for cleanliness of the process.

Gas pod is another part of this unit where the flow of gases are automatically controlled by a programmable computer. Here, since the processed gas are flammable, the selection of flow lines are obtained by pneumatic valves which decrease the occurrence probability of electrical arcs in the case of a gas leakage. (as they operate under pressured air)

The flow rate of process gases are controlled at the desired value by mass flow controllers which uses TYLAN source technique where the flow rate is sensed by a mass flow meter linked to a computer.

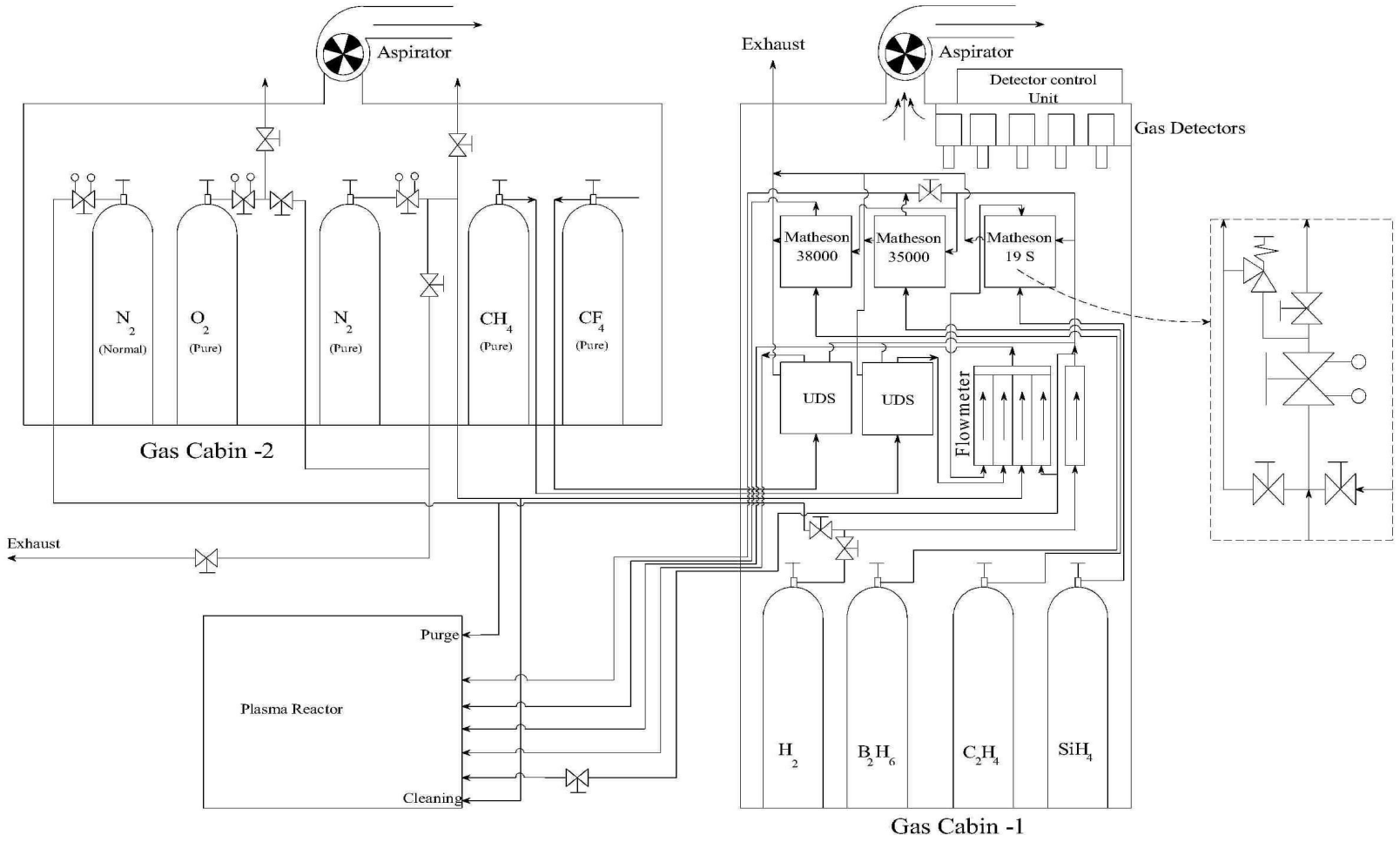

Figure 2.3: Gas cabinet system associated to the PECVD system.

2.1.3 Deposition Chamber

As the name implies, deposition chamber is the place where deposition occurs. Two electrodes constitute the main parameters of this unit. The distance between these electrodes are usually on the order of 40 mm or so. The plasma medium is generated in between.

Substrates are placed on the lower electrode, which is grounded and made of anodized aluminum.[2] The temperature of this electrode can be controlled between room temperature and 400°C. On the other hand, this electrode is fitted with a thermally resistive stand on a table which is cooled by water to protect o-ring[3] of the chamber wall.

The process gases are introduced into the plasma medium from the middle of the upper electrode which is made of aluminum and cooled with water during the process. This electrode is mounted by an hoist assembly which allows someone to change samples in short times. In order to provide a clean medium while loading and unloading the grown films or substrates, a glove box is allowed to cover the deposition chamber. Additionally, N_2 flow is supplied to this medium for maintaining inert atmosphere. Glove box has a load lock to prevent the atmosphere in the room to penetrate inside while placing the substrates.

[2] aluminum electrode is covered by anodized aluminum which serves as a thin insulating layer to protect the electrode surface.

[3] o-ring is the thin layer which serves to protect the vacuum medium.

2.1.4 Substrate Heating Assembly

Usually PECVD systems require a process temperature of about 500°C or even less. This temperature, which is necessary for the depositon process, is provided into the deposition chamber by heater coils which are placed in the bottom electrode.

2.1.5 Pumping System

PECVD system includes a roots blower type pump (booster) that is used for producing and maintaining the low pressure during the deposition process. It is capable of providing a vacuum pressure on the order of 10^{-3} Torr. Since its operation is based on an oil free principle it helps minimizing the impurity level at the exhaust. See Figure 2.4. Also a rotary type mechanical pump is used backing this pump, to facilitate the removal of all residuals.

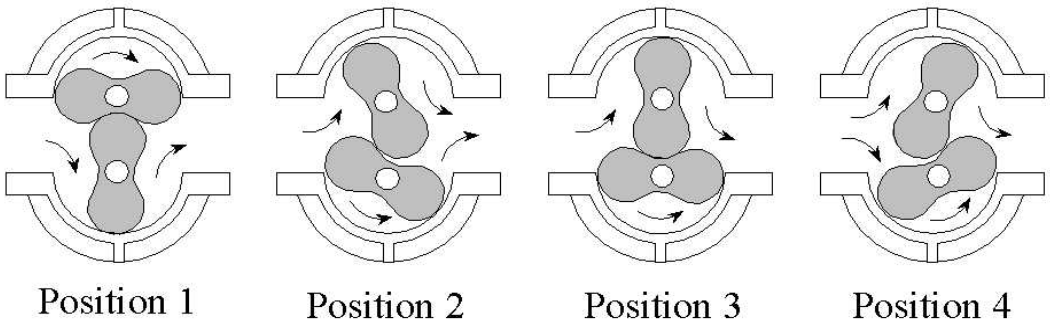

Figure 2.4: Operation of a Roots Blower Pump
Two eight-figured lobe impellers mounted on parallel shafts rotate in opposite directions. As each impeller passes the blower inlet, it traps a definite volume of air and carries it around the case to the blower outlet, where the air is discharged. Timing gears control the relative position of the impellers to each other, which allows operation without lubrication inside the air casing.

2.2 UV-Visible Spectrometer (Perkin Elmer Lambda 2S)

Perkin Elmer Lambda 2S Spectrometer was used for transmission and reflection measurements. It is a double beam spectrometer for ultraviolet-visible region having the wavelength range of 200-1100 nm. A deuterium and a tungsten-halogen lamp are used as radiation sources. As the output, it provides with the transmission values of any sample over 100% percent within the required wavelength range. A sample output is given in Figure 2.5 below. The optical path of the system is illustrated in figure 2.6 on the next page.

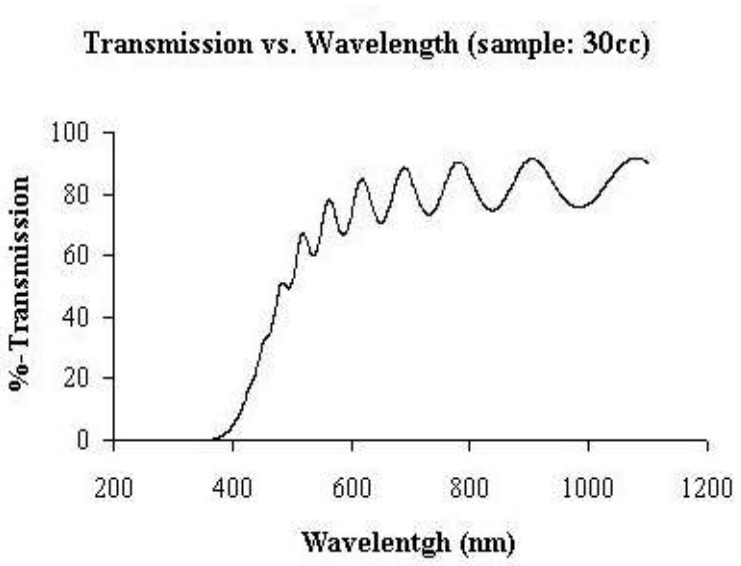

Figure 2.5: A sample output of UV-VIS Spectrometer Lambda 2S. This is transmission spectrum of a glass sample (corning), coated by a-$Si_{1-x}C_x$:H thin film.

The monochromator is a concave holographic grating with 1053 lines/mm. A movable planar mirror P1 is positioned by a mechanical arm to block the light emerging from one of the two light sources (DL or HL, which provide ultraviolet radiation and visible radiation respectively), and the light emerging from

the other source is reflected onto the toroidal mirror T2. Source changes due to the positioning of mirror P1 occur in synchronization with the monochromator. The monochromator stops slewing (rotating) until the source change is complete. Radiation, focused by T2 onto the entry slit ES1, first passes through some filters (FW) to limit the wavelength range reaching to the monochromator, hence reducing the stray radiation. Namely, the filter wheel rotates different optical filters into the radiation beam. It is synchronized with the monochromator. As the light beam reaches to the monochromator, it is spectrally dispersed and focused on the exit slit ES2. After the light beam passes through a spherical mirror S3, it is reflected onto the beam splitter BS which allows %50 of the light to pass through the planar mirror P4, and the other %50 portion to be reflected onto the planar mirror P5. Mirror P4 focusses the radiation beam in the sample cuvette. The radiation is then focused onto the sample photo-diode detector by a simple convex lens. Mirror P5 focuses the radiation beam in the reference cuvette. The radiation is then focused onto the reference photo-diode detector by a simple convex lens. [16]

For reflectance measurements the reflectance unit shown in Figure 2.6 needs to be positioned onto the sample platform. Reflectance measurements at approximately normal angle of incidence are performed first with a calibrating mirror in place of the sample, and then with the sample.

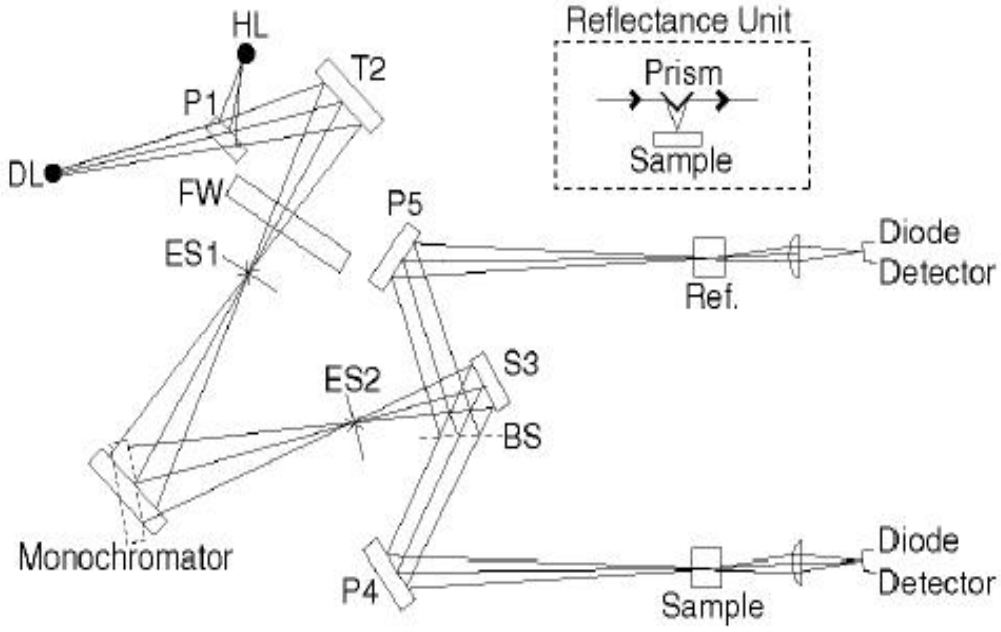

Figure 2.6: The optical path of the Perkin Elmer Lambda 2 Spectrometer. [16] Reflectance unit is positioned on the sample platform for reflectance measurements.

2.3 Fourier Transform Infrared (FT-IR) Spectroscopy

In infrared spectroscopy, IR radiation is passed through a sample. Some of the infrared radiation is absorbed by the sample and some of it is passed through (transmitted). The resulting spectrum represents the molecular absorption and transmission, creating a molecular fingerprint of the sample. Like a fingerprint no two unique molecular structures produce the same infrared spectrum.

Attainments of IR spectroscopy can be resumed as follows:

- It can identify unknown materials
- It can determine the quality or consistency of a sample

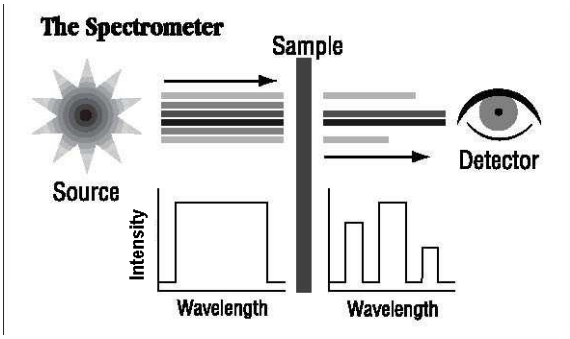

Figure 2.7: Spectroscopy

• It can determine the amount of components in a mixture

Fourier transform infrared spectroscopy is preferred over dispersive or filter methods of infrared spectral analysis for several reasons:

• It is a non-destructive technique.

• It provides a precise measurement method which requires no external calibration

• It can increase speed, collecting a scan every second

• It can increase sensitivity – one second scans can be co-added together to ratio out random noise

• It has greater optical throughput

• It is mechanically simple with only one moving part

A simple layout of an actual spectrometer is represented in the Figure 2.8.

The unusual and most important part of spectrometer 'interferometer' is treated particularly in the next section.

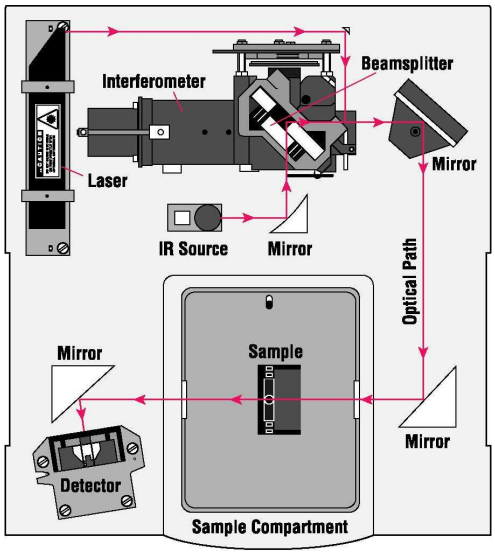

Figure 2.8: FT-IR Spectroscopy Layout

2.3.1 Michelson Interferometer

The Michelson interferometer, first introduced by Albert Michelson in 1881, has played a vital role in the development of modern physics. This simple and versatile instrument was used, for example, to establish experimental evidence for the validity of the special theory of the relativity, to measure the tidal effect of the moon on the earth and to provide a substitute standard for the "meter" in terms of wavelengths of lights.

A simple sketch of Michelson interferometer is shown in Figure 2.9. From an extended source of light (usually a laser), a beam of light is split by beam splitter by means of a thin, semitransparent front surface metallic or dielectric film, deposited on glass. Reflected beam 1 and transmitted beam 2, of roughly equal amplitudes, continue to fully reflecting mirrors S_1 and S_2, respectively, and where their directions are reversed. On the returning to the beam splitter, beam

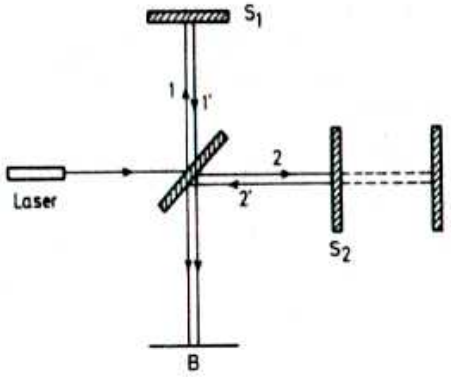

Figure 2.9: Simple layout of a Michelson interferometer

1 is now transmitted and beam 2 is reflected by the semitransparent film so that they come together again and leave the interferometer. Resulting beam include rays that traveled different optical paths and will demonstrate interference. If one of the mirrors is made movable, the difference between optical paths of beams 1 and 2 can be gradually varied. Introduced phase difference can be seen easily to be:

$$\Delta\theta = 2\pi\frac{2\Delta d}{\lambda} \tag{2.1}$$

Where Δd is the displacement of the movable mirror from the distance of the fixed mirror.

Importance of the easiness in the control of the phase difference will be understood well in the treatment of the FT-IR process, in next section.

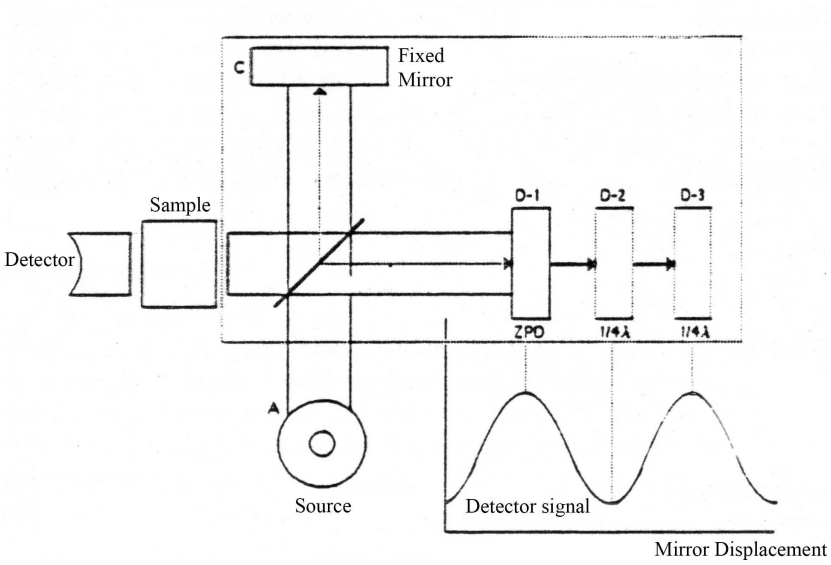

Figure 2.10: Schematic view of an FT-IR spectrometer.

2.3.2 FT-IR Spectrometer (Nicolet 520)

Structural analysis of a-$Si_{1-x}C_x$:H films is performed by FT-IR transmission spectrometer, Nicolet 520.

The FT-IR spectrometer has three basic components:

- a source
- a Michelson interferometer
- a detector

Collimated radiation from the broadband infrared source is directed into the interferometer. The resulting beam from interferometer, which shows constructive and destructive interference depending on the position of the moving mirror relative to the fixed mirror, passes through (or reflects from) the sample where selective absorption takes places, and continues to the detector. The "scan" in

FT-IR spectroscopy is the mechanical displacement of the moving mirror assembly; not a scan of individual frequencies as with a monochromator type system.

Consider the detector response for a single frequency component from the infrared source. This simulates a monochromatic source, for example, a laser. The single frequency beam passes through the beam-splitter. The resulting two beams move through a sequence of constructive and destructive interference, depending on the position of the moving mirror relative to the fixed mirror.

1. Constructive Interference: Δd=0

   When the position of the moving mirror is such that the distance between the beam-splitter and this mirror is exactly the same as the distance between the beam-splitter and the fixed mirror, the two reflected beams pass through exactly the same path length and, consequently, are totally in phase with each other. As a result, the two beams interfere constructively and the detector observes a maximum signal intensity. This position of the moving mirror is called the point of 'Zero Path Difference', or ZPD.

2. Destructive Interference: Δd= 1/4λ

   As the mirror moves away from the ZPD, Δd starts to increase from 0. When the distance between the beam-splitter and the moving mirror is 1/4 of the wavelength of light longer than that distance between the beam-splitter and the fixed mirror, two beam turn out be out of phase by π radian by Eqation 2.1 and at this point in the scan, two beam interfere with each other destructively, causing a minimum in the detector response.

3. Destructive/Constructive/Destructive: Δd= n x 1/4λ

   With each 1/4 wavelength displacement, this pattern of constructive and destructive interference repeats itself. Since data sampling occurs continuously, a cosine wave results, like the one shown in Figure 2.11

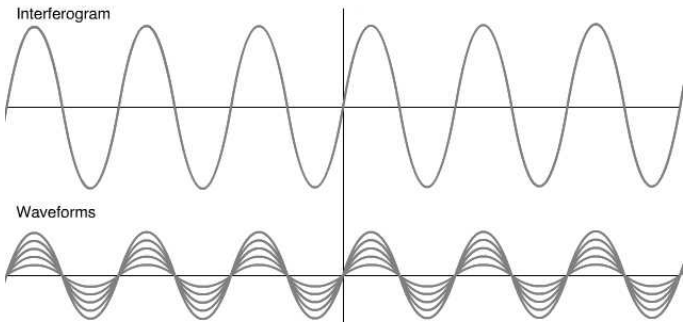

Figure 2.11: Interferogram of a single frequency

It is established that radiation of a single frequency results in an interference pattern that is a cosine wave by the interferometric technique. However, this is a modulated or modified cosine wave whose frequency is determined by the velocity of the moving mirror. Higher the velocity, higher the frequency of the modulated cosine functions. Mathematically, the Fourier transformation of a single frequency is a cosine wave. Therefore, the interferometer is actually taking the Fourier transform of the incoming signal.

This same process occurs for every frequency emitted from the broadband infrared source. When multiple frequencies are sampled at once, the resulting signal observed by the detector is the signed summation of the individual modulated cosine waves. This type of signal, shown in Figure 2.12, is called an interferogram or time domain spectrum (intensity versus time within the mirror scan).

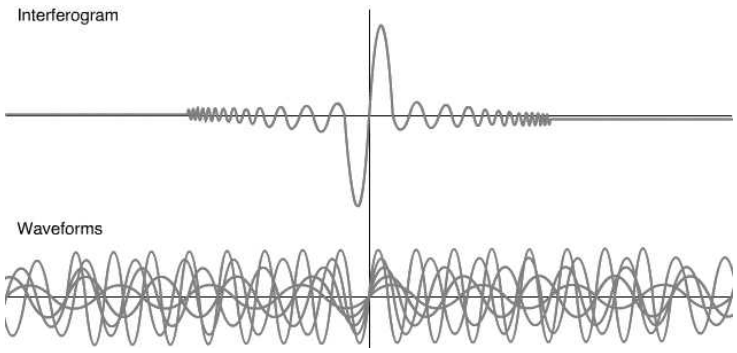

Figure 2.12: Interferogram of multiple frequencies.

Resolution in an FT-IR system is defined by the length of mirror travel beyond the ZPD point. The further the mirror travels, the higher the resolving power of the instrument.

This phenomenon occurs because the Fourier transformation can only distinguish two different frequencies if there is a difference in their modulated cosine waves. If two frequencies are very similar, the resulting cosine waves will also be similar. Only a longer mirror travel can pick out the subtle differences.

In summary, the interferometer encodes the initial frequencies (by optically taking the Fourier transformation of the incoming signal) into a special form that the detector can observe in time. The inverse Fourier transformation is a mathematical means of resorting the individual frequencies for the final presentation of the infrared spectrum. In other words, a Fourier transformation simply converts from one domain into another; in this case, from the time domain (measured) to the frequency domain (desired). It is this final spectrum that interests the infrared spectroscopists.

It is important to remember that any data point of the interferogram represents the summation of components from each modulated frequency. Each data point contains information over the entire infrared region to which the detector is sensitive. In reality, the detector observes all frequencies simultaneously. [45]

2.3.3 Sampling Techniques

2.3.3.1 Transmission Spectroscopy:

This technique can be used for solid, liquid, and gas sampling. Here, light is passed through the sample and compared to light that has not. The resulting spectrum depends on the path length or sample thickness, the absorption coefficient of the sample, the reflectivity of the sample, the angle of incidence, the polarization of the incident radiation, and, for particulate matter, on particle size and orientation.

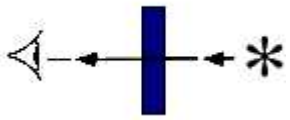

Figure 2.13: Transmission technique.

2.3.3.2 External Reflection Spectroscopy:

In this technique, also known as specular reflectance, light is reflected from a smooth (mirror-like) sample to record its spectrum. External reflectance is a non-destructive, non-contact technique. It is particularly useful for film thickness

and refractive index measurements, as well as recording spectra of thin films on metal substrates.

External reflection spectra may look different from transmission spectra in many ways, *e.g.* bands may be shifted to higher wave numbers, spectra may follow the dispersion in the refractive index, and spectral contrast may not depend linearly on sample thickness. There exist also other sampling techniques

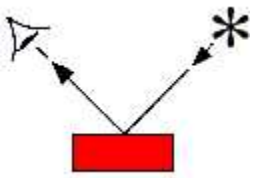

Figure 2.14: External reflection technique.

like Internal Reflection Spectroscopy, Diffuse Reflection Spectroscopy, Emission Spectroscopy, Photoacoustic Spectroscopy but they are not treated since they are out of the scope of our work.

CHAPTER 3

THEORY OF ULTRAVIOLET-VISIBLE LIGHT ABSORPTION

A light wave is described by its electric field $\vec{E}$ and magnetic induction $\vec{B}$. The electric field is expressed by the equation

$$\vec{E} = \vec{E}_o e^{j(wt-\vec{k}\cdot r)} \tag{3.1}$$

where w is the angular frequency and $\vec{k}$ is the wave vector $k = 2\pi/\lambda$. The magnetic induction $\vec{B}$ which has zero divergence ($\nabla \cdot \vec{B} = 0$) can be represented by the curl of a vector potential $\vec{A}$

$$A(r,t) = \vec{A}_o e^{j(wt-\vec{k}\cdot r)} \tag{3.2}$$

In Gauss system the vector potential $\vec{A}$ is introduced to describe $\vec{A}$ and $\vec{B}$

$$\vec{E} = -\frac{1}{c}\frac{\partial \vec{A}}{\partial t} \quad ; \quad \vec{B} = \nabla \times \vec{A} \quad \text{with} \quad \nabla \times \vec{A} = 0 \tag{3.3}$$

The Hamiltonian H_o of an electron inside a crystal is given by

$$H_o = \frac{\hat{p}^2}{2m} + U(r) \tag{3.4}$$

where $\hat{p}$ is the electron momentum and U(r) represents the crystal potential with the same periodicity as the crystal; meaning that it has the same values at equal intervals. Because of this periodicity, momentum of the crystal has some different features than the momentum of a free electron. The conservation of the

momentum of an electron in the crystal is satisfied by the quasimomentum (P). The relation between energy and quasimomentum is important to characterize the crystal. To express this relation, we need to express mass in terms of effective mass (m^*). In this case, the electron motion can be represented by a Bloch Wave (Ψ)

$$\Psi_k(r) = \varphi_k^o e^{j\vec{k}\cdot\vec{r}} \quad \text{where} \quad \vec{k} = \pm\sqrt{\frac{2m^*E}{\hbar^2}} \quad and \quad (m^*)^{-1} = \frac{d^2E}{dp^2} \tag{3.5}$$

The uncertainty in the displacement of the electron in the crystal is equal to the volume of the crystal, because the electron can be anywhere in the crystal. According to Heisenberg uncertainty relation ($\Delta x \Delta P \approx \hbar$), if the volume of the crystal is very large, the error in the momentum goes to zero. So, to define the states of an electron in a crystal, momentum space is preferred. The sub-index "k" in the wavefunction $\Psi_k(r)$ denotes that we work in momentum space.

Under illumination, Hamiltonian of an electron in the crystal changes. Substituting the momentum operator in the Hamiltonian gives

$$H = -\frac{\hbar^2\nabla^2}{2m} + U(r) + \frac{j\hbar e}{2mc}(\vec{A}\cdot\nabla) + \frac{e^2\vec{A}^2}{2mc^2} \tag{3.6}$$

neglecting the small term $\frac{e^2\vec{A}^2}{2mc^2}$

$$H \approx H_o + W \quad \text{where} \quad W = \frac{j\hbar e}{2mc}(A\cdot\nabla) \tag{3.7}$$

W is the perturbation to the Hamiltonian due to illumination. The wavefunction that represents the solution of the Hamiltonian can be separated to time and spatial components if (only if) the potential U(r) is time independent

$$\Psi_k^o(\vec{r},t) = \Psi_k(\vec{r})\chi(t)$$

where $\Psi_k^o(\vec{r},t)$ represents the wavefunction for the case when there is no illumination. Inserting this wavefunction into Schrödinger equation $j\hbar\frac{\partial}{\partial t}\Psi_k^o(\vec{r},t) = \hat{E}_k^o\Psi_k^o(\vec{r},t)$ gives

$$\chi(t) = e^{-j\frac{E^o(k)t}{\hbar}} \tag{3.8}$$

If at t=0 the illumination $W = \frac{j\hbar e}{2mc}(A\cdot\nabla)$ is applied to the sample as a perturbation, the wavefunction modifies to the new conditions as

$$\Psi_k(\vec{r},t) = \int c(t)\Psi_k^o(\vec{r},t)dk \tag{3.9}$$

If this wavefunction is substituted into the time dependent Schrödinger equation, and both sides are multiplied by $\Psi_{k'}^o(\vec{r},t)$ (complex conjugate of $\Psi_k^o(\vec{r},t)$) the Schrödinger equation will result

$$i\hbar\frac{d}{dt}c_{k'} = \int c_k(t)e^{j\omega_{k'k}t}W_{k'k}dk \tag{3.10}$$

where

$$W_{k'k} = \frac{E(k') - E^o(k)}{\hbar} \tag{3.11}$$

and

$$W_{k'k} = \int \Psi_{k'}^{o^*}(\vec{r})\hat{W}\Psi_k^o(\vec{r})d\tau$$

The solution of (3.10) is not obvious, but an approximate solution can be found by perturbation method if $\hat{W}$ is small enough. The coefficient $c_k(t)$ may be developed into series around c_k^o corresponding to $\hat{W} = 0$ ($\hat{W} = 0$ before illumination). Then;

$$c_k(t) = c_k^o(t) + c_k^1(t) + c_k^2(t) + ... \tag{3.12}$$

At the moment t=0, just before the application of the perturbation $\hat{W}$, assume that system is at one of the stationary state $\Psi^o_{k''}(\vec{r},t)$ corresponding to the energy $E^o(k^{''})$. In the relation (3.9) all $c_k = 0$ except $c_{k''}$ then

$$c_k = \delta(k - k^{''}) \tag{3.13}$$

So (3.10) becomes (retaining only the 1^{st} order terms)

$$i\hbar \frac{d}{dt} c^{(1)}_{k'}(t) = \int \delta(k - k'') e^{i\omega_{k'k}t} W_{k'k} dk \tag{3.14}$$

$$= W_{k'k''} e^{i\omega_{k'k''}t} \tag{3.15}$$

solving this integral one obtains

$$c^{(1)}_{k'}(t) = \frac{1}{i\hbar} \int_0^{t_o} W_{k'k''} e^{i\omega_{k'k''}t} dt \tag{3.16}$$

so

$$\left| c^{(1)}_{k'}(t) \right|^2 = \frac{1}{\hbar^2} \left| \int_0^{t_o} W_{k'k''} e^{i\omega_{k'k''}t} dt \right|^2 \tag{3.17}$$

This relation is interpreted as the "transition probability" from the state $\Psi^o_{k''}(\vec{r},t_o)$ to the state $\Psi^o_{k'}(\vec{r},t_o)$ under the action of perturbation $\hat{W}$ during the time duration t_o [36]. Utilizing (3.17), we can define the transition rate (photon absorption probability per unit time) as

$$M(k'' \rightarrow k') = \left| \frac{d}{dt} c^{(1)}_{k'}(t) \right|^2 \tag{3.18}$$

Substituting (3.11), (3.12), (3.13), and (3.17) into (3.18) provides us with

$$M(k'' \rightarrow k') = \frac{2eA_o^2}{m^2c^2\hbar^2} \left| \int \varphi^{o^*}_{k'}(r) e^{-j[\vec{k}' - \vec{k}]\cdot\vec{r}} (\vec{a}_o \cdot \vec{p}) \varphi^o_{k''}(r) e^{j\vec{k}''\cdot\vec{r}} d\tau \right|^2 \sin \frac{(\omega_{k'k''} - \omega)t}{\omega_{k'k''} - \omega} \tag{3.19}$$

where $\vec{a}_o$ is the unit vector along the vector potential amplitude $\vec{A}^o$, and $\vec{a}_o \cdot \vec{p}$ is the component of the momentum along the vector potential $\vec{A}$.

3.1 Conservation of Momentum

In the transition probability Equation 3.19, the middle term with absolute square indicates the momentum based quantities, which can be utilized to prove conservation of quasimomentum of a system. Let us designate this middle term as

$$|P_{k'k''}| = \left| \int \varphi^{o^*}_{k'}(r) e^{-j[\vec{k}'-\vec{k}]\cdot\vec{r}} (\vec{a}_o \cdot \vec{p}) \varphi^o_{k''}(r) e^{j\vec{k}''\cdot\vec{r}} d\tau \right| \tag{3.20}$$

Considering the case of effective mass approximation where the amplitude of the Bloch function given by $\Psi^o_k(\vec{r}) = \varphi^o_k(\vec{r}) e^{j\vec{k}\cdot\vec{r}}$, where $\varphi^o_k(\vec{r}) = constant = \varphi^o$ then

$$\Psi^o_k(\vec{r}) = \varphi^o(\vec{r}) e^{j\vec{k}\cdot\vec{r}} \tag{3.21}$$

normalizing this function gives

$$\int \Psi^o_{k'}(\vec{r}) \Psi^o_k(\vec{r}) d\tau = \delta_{kk'} = \int |\varphi^o|^2 d\tau \Rightarrow |\varphi^o|^2 \tau = 1 \Rightarrow \varphi^o = \frac{1}{\sqrt{\tau}} \tag{3.22}$$

$$\Psi^o_k(\vec{r}) = \frac{1}{\sqrt{\tau}} e^{j\vec{k}\cdot\vec{r}} \tag{3.23}$$

Using (3.23), (3.20)

$$\begin{aligned} P_{k'k''} &= \int \frac{1}{\sqrt{\tau}} e^{-j([\vec{k}'-\vec{k}]\cdot\vec{r})} (\vec{a}_o \cdot \vec{p}) \frac{1}{\sqrt{\tau}} e^{j\vec{k}''\cdot\vec{r}} d\tau & (3.24) \\ &= \frac{h}{\tau} \left(\vec{a}_o \cdot \vec{k}'' \right) \int e^{-j([\vec{k}'-k''-\vec{k}]\cdot\vec{r})} d\tau & (3.25) \\ &= h \left(\vec{a}_o \cdot \vec{k}'' \right) \delta([\vec{k}' - \vec{k}], \vec{k}'') & (3.26) \end{aligned}$$

This matrix element is nonzero only if $\vec{k}' - \vec{k} = \vec{k}''$. So

$$\vec{k}' = \vec{k}'' + \vec{k} \tag{3.27}$$

If the perturbation is small, the magnitude of $\vec{k}$ is also small. So we can assert that

$$\vec{k'} \cong \vec{k''} \tag{3.28}$$

which is known as dipole approximation, and reflects the quasimomentum conservation of the system [37, 38].

3.2 Conservation of Energy

In the transition probability equation (3.19) the last term with sine function indicates the energy based quantities. Now, let us do such substitutions for the terms in sine function; let $\omega_{k'k''} - \omega \equiv \beta$ and $\beta t_o \equiv x$. Then the sine term is modified in the following way

$$\frac{t_o \sin(\omega_{k'k''} - \omega)t_o}{\beta t_o} \longrightarrow \frac{t_o \sin(\beta t_o)}{\beta t_o} = I \longrightarrow \lim_{\beta \to 0} I = t_o \tag{3.29}$$

The absorption probability, which is directly proportional to I, fluctuates in 2π period and attenuates in both directions in magnitude, as seen in Figure 3.1. The maximum absorption is obtained between $-\pi$ and π. As seen in the graph of this function I is only within the interval $\Delta\beta = \frac{2\pi}{t_o}$. For $t_o \to \infty$ (large), I resembles δ (delta) function.

$$t_o \to \infty \quad \longrightarrow \quad \Delta\beta \to 0 \quad \longrightarrow \quad I \to \infty \tag{3.30}$$

So that

$$\int_{-\infty}^{+\infty} I d\beta = \pi \quad \Rightarrow \quad \frac{\sin(\beta t_o)}{\beta} \frac{1}{\pi} \approx \delta(\beta) \quad \Rightarrow \quad \delta(\hbar\beta) = \frac{1}{\hbar}\delta(\beta) \tag{3.31}$$

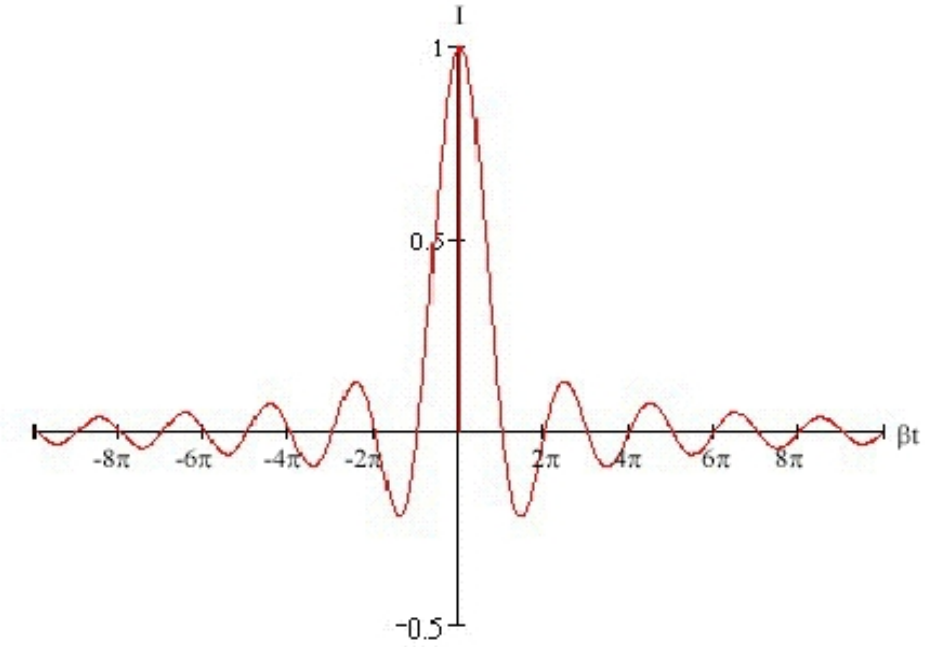

Figure 3.1: I versus βt_o

Combining the terms above

$$\frac{\sin \beta t_o}{\beta} \approx \delta(\beta)\pi = \hbar\delta(\hbar\beta)\pi = \hbar\pi\delta(\hbar\beta) \tag{3.32}$$

The transition is probable if $\delta(\beta)$ is nonzero, and $\delta(\beta)$ is nonzero only if $\beta = 0$. If $\beta = 0 \Rightarrow \hbar\beta = 0$. Then we have $E_c^o(k') - E_v^o(k'') = \hbar\omega$. Inserting this last term in $M_{k''\to k'}$ gives

$$M_{k''\to k'} = \frac{2\pi}{\hbar}\frac{e^2 A_o^2}{m^2 c^2}\left|P_{k'k''}\right|^2 \delta\left[E_c^o(k') - E_v^o(k'') - \hbar\omega\right] \tag{3.33}$$

Looking at the term in the delta function, we result in

$$E^o(k') = \hbar\omega + E^o(k'') \tag{3.34}$$

which expresses the conservation of energy.

3.3 Optical Absorption Coefficient α

Consider that a flux F_o of photons(number of photons per unit area per unit time interval) is incident on an absorbing semi conducting material, as depicted in Figure 3.2. The number of photons dn absorbed per unit time interval dt

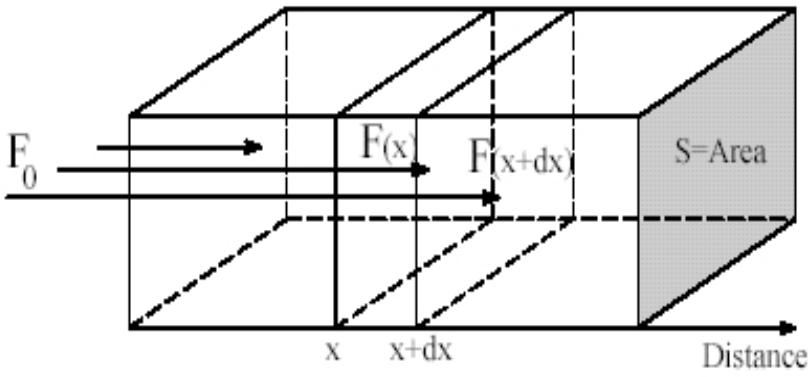

Figure 3.2: A photon flux F_o, incident on a semiconductor with a cross-sectional area S, is absorbed by that semiconductor

within the elementary volume ($dV = Sdx$) is

$$\begin{aligned} dn(x) &= [F(x) - F(x+dx)]S \qquad (3.35) \\ &= -[F(x+dx) - F(x)]\frac{dx}{dx}S \\ &= -\{\frac{F(x+dx) - F(x)}{x+dx-x}\}dxS \\ &= -\frac{dF(x)}{dx}dxS \\ &= -dF(x)S \qquad (3.36) \end{aligned}$$

or in differential form;

$$\frac{1}{S}\frac{dn(x)}{dx} = -\frac{dF(x)}{dx} \qquad (3.37)$$

Absorption cross-section σ is defined as [39]

$$\sigma = \frac{\text{Energy absorbed by an absorbing atomic center / unit time}}{\text{Energy flux of radiation}}$$

σ can be interpreted as probability of an absorption (transition between one empty and one filled state) per one photon of energy $\hbar\omega$ by a single absorbing atomic center per unit time [40]. Total absorption cross-section per unit volume is $N\sigma$ where N is the concentrations of absorbing atomic centers per unit volume. The number of photons absorbed per unit time, per unit volume is

$$\frac{1}{S}\frac{dn}{dx} = \sigma N F(x) \tag{3.38}$$

Combining 3.37 and 3.38, we have

$$dn = \sigma F(x) N S dx = -dF(x) S \tag{3.39}$$

simplifying 3.39, we obtain

$$\frac{dF(x)}{F(x)} = -\sigma N dx \tag{3.40}$$

It is seen that, dn is also proportional to

- σ : cross section area of each absorbing atomic center.
- $dN = NdV = NSdx$: the number of absorbing atomic centers (in volume dV) with N being the concentration of these centers
- $F(x)$: average incoming flux towards this volume.

Integrating both sides of 3.40 gives us

$$\ln F(x) = -\sigma N x + contant$$

$$F(x) = F_o e^{-\alpha x} \quad \text{with} \quad \alpha = \sigma N \tag{3.41}$$

where α is named as "absorption coefficient". Flux $F(x)$ is decaying exponentially as it penetrates into the material.

3.4 Spectral Dependence of α

Energy density u of the incident light is

$$u = \frac{1}{8\pi} (E \cdot D + B \cdot H) \tag{3.42}$$

Time-averaged energy density is

$$\begin{aligned} u &= \frac{1}{16\pi} (E \cdot D^* + B \cdot H^*) \\ &= \frac{\left(n^2 + |N|^2\right) \varepsilon^2}{16\pi} \end{aligned}$$

where μ is assumed to be 1. Absolute square of the complex refractive index is

$$|N|^2 = n^2 + k^2$$

If $k^2 \ll n^2$ is valid over the most of the spectrum, the time-averaged energy density can be expressed in the following form;

$$u = \frac{n^2 \varepsilon^2}{8\pi}$$

If energy of the light in a volume Sdx is

$$\begin{aligned} U &= Sdx \frac{n^2 \varepsilon^2}{8\pi} \\ &= Svdt \frac{n^2 \varepsilon^2}{8\pi} \end{aligned}$$

energy of the light per unit area, per unit time can be written as

$$\begin{aligned} U &= v\frac{n^2\varepsilon^2}{8\pi} \\ &= \frac{c}{n}\frac{n^2\varepsilon^2}{8\pi} \\ &= \frac{cn\varepsilon^2}{8\pi} \end{aligned}$$

where the approximation $k^2 \ll n^2$ is used again for photon velocity v. Photon flux can be found from energy flux defined in Equation 3.43;

$$F = \frac{U}{\hbar\omega} \tag{3.43}$$

$$= \frac{cn\varepsilon^2}{8\pi\hbar\omega} \tag{3.44}$$

Using the relation between ε and A_o

$$\varepsilon = \frac{\omega}{c}A_o \tag{3.45}$$

photon flux can be expressed as

$$F = \frac{cn}{8\pi\hbar\omega}\frac{\omega^2 A_o^2}{c^2} \tag{3.46}$$

$$= \frac{\omega n A_o^2}{8\pi\hbar c} \tag{3.47}$$

Remembering that σ stands for the probability of transition per unit flux per unit time, and also that $M_{k''\to k'}$ is the transition probability per unit time for a flux F, σ can be related to $M_{k''\to k'}$ and F;

$$\sigma = \frac{M_{k''\to k'}}{F} \tag{3.48}$$

$$= \frac{8\pi\hbar c}{\omega n A_o^2} M_{k''\to k'} \tag{3.49}$$

Taking it another way, the transition probability M is both proportional to the cross section area and the flux.

The number of accessible electronic states between valence and conduction bands in the quasimomentum space (k-space) per unit volume in k can be found by using Heisenberg uncertainty principle

$$g(k)dk = \frac{d\tau_k}{4\pi^3} \tag{3.50}$$

where τ_k is the volume in three dimensional k-space corresponding to two electron states (spin up & spin down) The occupation probability of an electronic state, defined by the quasimomentum vector k, is given by the Fermi-Dirac distribution

$$f(k) = \frac{1}{e^{\frac{E^o(k)-E_F}{k_B t}} + 1} \tag{3.51}$$

where k_B is the Boltzman constant ($\simeq 1.3807{\cdot}10^{-23} J/K$). To find the number of states coupled between valence and conduction band states available for photon absorption, we combine (3.50) and (3.51) and find this number as

$$dN = f(k'')[1 - f(k')]\frac{d\tau_{k''}}{4\pi^3}\frac{d\tau_{k'}}{4\pi^3} \tag{3.52}$$

where $f(k'')$ is the initial state in the valence band which is filled, and $f(k')$ is the final state in the conduction band which is empty. Noting that $f(k'') \approx 1$ and $f(k') \approx 0$, dN approximately equals to

$$dN \approx \frac{d\tau_{k''}}{4\pi^3}\frac{d\tau_{k'}}{4\pi^3} \tag{3.53}$$

The absorption coefficient α can be expressed as the combination of (3.41), (3.49) and (3.53)

$$\alpha = \frac{8\pi\hbar c}{\omega n A_o^2} \iint\limits_{\tau_{k'}\tau_{k''}} M_{k''\to k'}\frac{d\tau_{k'}}{4\pi^3}\frac{d\tau_{k''}}{4\pi^3} \tag{3.54}$$

Substituting Equation 3.33 for $M_{k''\rightarrow k'}$ into equation (3.54), we end up with

$$\alpha = \frac{8\pi\hbar c}{\omega n A_o^2}\frac{2\pi}{\hbar}\frac{e^2A_o^2}{m^2c^2}\iint_{\tau_{k'}\tau_{k''}}|P_{k'k''}|^2\,\delta\left(E_c^o(k') - E_v^o(k'') - \hbar\omega\right)\frac{d\tau_{k'}}{4\pi^3}\frac{d\tau_{k''}}{4\pi^3} \quad (3.55)$$

$$= \frac{e^2}{\pi^4 wnm^2c}\iint_{\tau_{k'}\tau_{k''}}|P_{k'k''}|^2\,\delta\left(E_c^o(k') - E_v^o(k'') - \hbar\omega\right)d\tau_{k'}d\tau_{k''} \quad (3.56)$$

This expression is zero unless $k' = k'' + g$, which is the condition required for the conservation of momentum. So, neglecting g, Equation 3.56 becomes

$$\alpha = \frac{e^2}{\pi^4 wnm^2c}\int_{\tau_{k''}}\left|P_{k_c''k_v''}\right|^2\,\delta\left(E_c^o(k'') - E_v^o(k'') - \hbar\omega\right)d\tau_{k''} \quad (3.57)$$

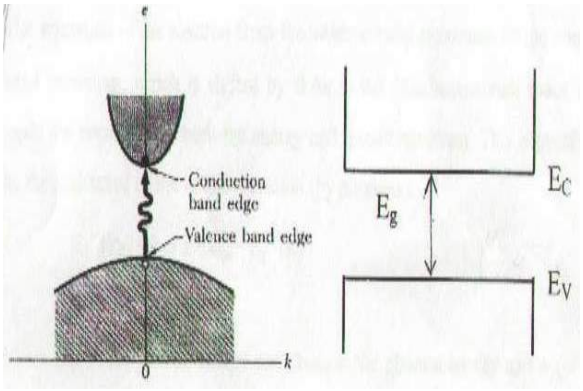

Figure 3.3: Direct Band Structure

Consider a semiconductor having a direct band structure as shown in Figure 3.3.

Assuming parabolic bands (which is a result of effective mass approximation)

gives the initial and final energies as

$$E_c(k'') = E_c + \frac{\hbar^2 k''^2}{2m_n^*} \tag{3.58}$$

$$E_v(k'') = E_v - \frac{\hbar^2 k''^2}{2m_p^*} \tag{3.59}$$

where E_v and E_c are valence band and conduction band edges, respectively. Choosing electron energy is zero at the top of the valence band [41], the conduction and valence band energies can be written as;

$$E_c(k'') = E_g + \frac{\hbar^2 k''^2}{2m_n^*} \tag{3.60}$$

$$E_v(k'') = -\frac{\hbar^2 k''^2}{2m_p^*} \tag{3.61}$$

where

$$E_g = E_c - E_v$$

Conservation of energy requires

$$\hbar\omega = E_c^o(k'') - E_v^o(k'') \tag{3.62}$$

$$= E_g + \frac{\hbar^2 k''^2}{2m_n} + \frac{\hbar^2 k''^2}{2m_p} \tag{3.63}$$

$$= E_g + \frac{\hbar^2 k''^2}{2m^*} \tag{3.64}$$

where m^* is the reduced mass of the electron-hole pair and defined as

$$m^* = \frac{m_n^* m_p^*}{m_n^* + m_p^*}$$

Using Equation 3.64 in Equation 3.57 gives

$$\alpha = \frac{e^2}{\pi^4 \omega n m^2 c} \int \left| P_{k_c'' k_v''} \right|^2 \delta \left(E_g + \frac{\hbar^2 k''^2}{2m^*} - \hbar\omega \right) d\tau_{k''} \tag{3.65}$$

Because of the direct band structure, the maxima of the valence band and conduction band are located at the point $k'' = 0$. So we can expand the matrix element $P_{k_c'' k_v''}$ in Equation 3.65 around $k'' = 0$ as follows

$$P_{k_c'' k_v''} = P_{0_c 0_v} + \frac{P_{k_c'' k_v''(k''=0)}}{dk''} dk'' + ... \tag{3.66}$$

Assuming that the zero order term $P_{0_c 0_v} \neq 0$ and neglecting the higher order expansion terms

$$P_{k_c'' k_v''} \approx P_{0_c 0_v} \tag{3.67}$$

Then, α can be expressed as

$$\alpha = \frac{e^2}{\pi^4 \omega n m^2 c} \left| P_{0_c 0_v} \right|^2 \int 4\pi k'' dk'' \delta \left(E_g + \frac{\hbar^2 k''^2}{2m^*} - \hbar\omega \right) \tag{3.68}$$

Setting $u = \frac{\hbar^2 k''^2}{2m^*}$, the integral can be expressed in following form;

$$\alpha = \frac{2e^2}{\pi^3 \omega n m^2 c} \left| P_{0_c 0_v} \right|^2 \left(\frac{2m^*}{\hbar^2} \right)^{3/2} \int u^{1/2} du \delta \left(u - (\hbar\omega - E_g) \right) \tag{3.69}$$

After taking the integral, we have

$$\alpha = \frac{2e^2}{\pi^3 \omega n m^2 c} \left| P_{0_c 0_v} \right|^2 \left(\frac{2m^*}{\hbar^2} \right)^{3/2} (\hbar\omega - E_g)^{1/2} \tag{3.70}$$

α can be expressed in a simple form as [42]

$$\alpha = \beta \left(\frac{\sqrt{\hbar\omega - E_g}}{\hbar\omega} \right) \tag{3.71}$$

where

$$\beta = \frac{2e^2}{\pi^3 n m^2 c \hbar^2} \left| P_{0_c 0_v} \right|^2 (2m^*)^{3/2} \tag{3.72}$$

3.5 Transmission and Reflection of a Thin Film on a Substrate

Assume that a beam is incident on a thin film which has parallel-plane boundaries sandwiched between air and infinitely long transparent ($\kappa = 0$) substrate as shown in Figure 3.4. The film has a complex refractive index N with a thickness d. The air and substrate has refractive indices 1 and n_s, respectively. The beam is divided into reflected and transmitted parts at each interface. Incident wave is reflected and some part of it is transmitted at the air-film interface. The transmitted wave inside the film is multiply-reflected and multiply-transmitted at the film-substrate and film-air interfaces. Amplitudes of the transmitted and reflected beams are obtained by summing the Fresnel coefficients of multiply-reflected and multiply-transmitted beam elements [26]. The multiply-reflected and multiply-transmitted beams can be written in terms of Fresnel coefficients. Fresnel reflection and transmission coefficients at the air-film and film-substrate interfaces are denoted by r_1, t_1 and r_2, t_2, respectively. The corresponding coefficients for propagation from the film to the air are r_1' and t_1'. As the wave traverses the film from one boundary to the other, a constant phase change is added to its phase. In terms of the free-space wavelength λ, d, N and the angle of refraction r, the phase change is given by

$$\delta = \frac{2\pi}{\lambda} N_1 d \cos r \tag{3.73}$$

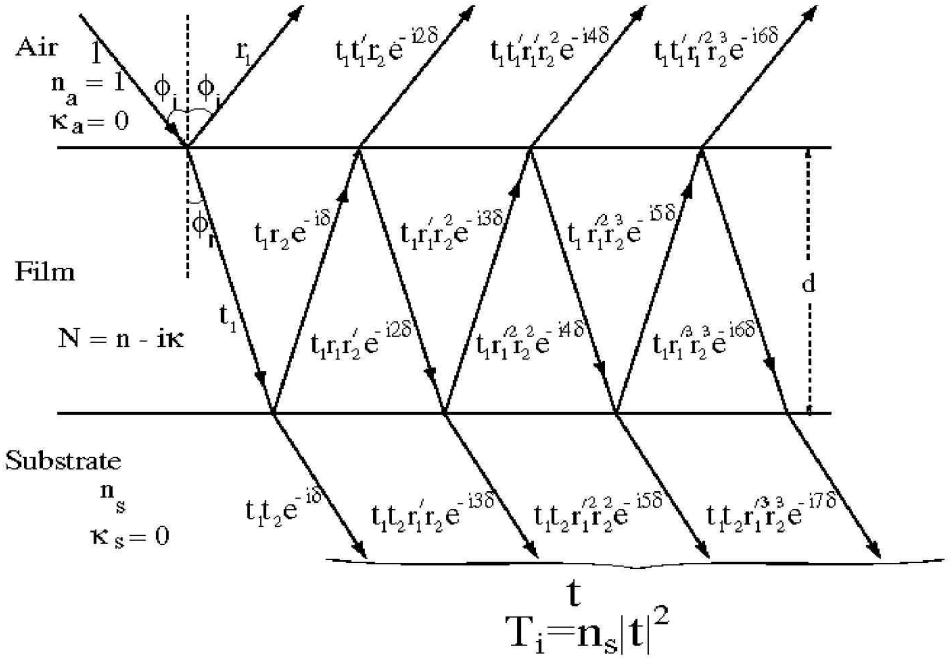

Figure 3.4: Multiple reflections and transmissions of a plane wave by an air-film-substrate system with parallel-plane boundaries. [28]

The transmitted amplitude is obtained by adding the partial waves;

$$\mathbb{T} = t_1 t_2 e^{-i\delta} + t_1 t_2 r_1' r_2 e^{-i3\delta} + t_1 t_2 r_1'^2 r_2^2 e^{-i5\delta} + ... \tag{3.74}$$

$$= t_1 t_2 e^{-i\delta} \underbrace{\left(1 + r_1' r_2 e^{-i2\delta} + r_1'^2 r_2^2 e^{-i4\delta} + ...\right)}_{\text{geometric series}} \tag{3.75}$$

$$= \frac{t_1 t_2 e^{-i\delta}}{1 - r_1' r_2 e^{-i2\delta}} \tag{3.76}$$

Using relative amplitudes [27], it can be shown that

$$r_1' = -r_1 \tag{3.77}$$

$$t_1' = \frac{1 - r_1^2}{t_1} \tag{3.78}$$

and with Equation 3.77 transmitted amplitude becomes

$$\mathbb{T} = \frac{t_1 t_2 e^{-i\delta}}{1 + r_1 r_2 e^{-i2\delta}} \tag{3.79}$$

Similarly, reflected amplitude is given by geometric series

$$\begin{aligned}
\mathbb{R} &= r_1 + t_1 t_1' r_2 e^{-i2\delta} + t_1 t_1' r_1' r_2^2 e^{-i4\delta} + t_1 t_1' r_1'^2 r_2^3 e^{-i6\delta} + ... \\
&= r_1 + t_1 t_1' r_2 e^{-i2\delta} \underbrace{\left(1 + r_1' r_2 e^{-i2\delta} + r_1'^2 r_2^2 e^{-i4\delta} + ...\right)}_{\text{geometric series}} \\
&= r_1 + \frac{t_1 t_1' r_2 e^{-i2\delta}}{1 - r_1' r_2 e^{-i2\delta}}
\end{aligned}$$

Using Equations 3.77 and 3.78, reflected amplitude takes the form

$$\mathbb{R} = \frac{r_1 + r_2 e^{-i2\delta}}{1 + r_1 r_2 e^{-i2\delta}} \tag{3.80}$$

Fresnel coefficients and reflection coefficients at the air-film interface and film-substrate interface for normal incidence are

$$t_1 = \frac{2}{1 + n - i\kappa} \tag{3.81}$$

$$t_2 = \frac{2\,(n - i\kappa)}{n - i\kappa + n_s} \tag{3.82}$$

$$r_1 = \frac{1 - n + i\kappa}{1 + n - i\kappa} \tag{3.83}$$

$$r_2 = \frac{n - i\kappa - n_s}{n - i\kappa + n_s} \tag{3.84}$$

If these coefficients are substituted into Equation 3.79

$$\begin{aligned}
\mathbb{T} &= \frac{\frac{4(n-i\kappa)}{(1+n-i\kappa)(n-i\kappa+n_s)} e^{-i2\pi Nd/\lambda}}{1 + \frac{1-n+i\kappa}{1+n-i\kappa}\frac{n-n_s-i\kappa}{n+n_s-i\kappa} e^{-i4\pi Nd/\lambda}} \\
&= \frac{4\,(n - i\kappa)\, e^{-i2\pi Nd/\lambda}}{(1 + n - i\kappa)\,(n + n_s - i\kappa) + (1 - n + i\kappa)\,(n - n_s - i\kappa)\, e^{-i4\pi Nd/\lambda}}
\end{aligned}$$

is obtained.

Transmittance, which is the ratio of transmitted to incident intensity is expressed by the relation

$$T = n(\frac{\cos\theta_t}{\cos\theta_i})t^2 \tag{3.85}$$

where θ_t and θ_i are angles of incidence and transmittance, respectively [29]. n is relative refractive index. Notice that T is not simply t^2 since it must take into account a different speed and direction in a new medium (film).

For normal incidence Equation 3.85 reduces to

$$T = nt^2 \tag{3.86}$$

So, in our case, transmittance is obtained by

$$\begin{aligned} T_i &= \frac{n_s}{n_{air}} |\mathbb{T}|^2 \\ &= \frac{n_s}{1} \mathbb{T}\mathbb{T}^* \end{aligned}$$

$$= \frac{16n_s \left(n^2+\kappa^2\right) e^{-4\pi\kappa d/\lambda}}{\left[(n+1)^2+\kappa^2\right]\left[(n+n_s)^2+\kappa^2\right] + Ce^{-4\pi\kappa d/\lambda} + \left[(1-n)^2+\kappa^2\right]\left[(n-n_s)^2+\kappa^2\right] e^{-8\pi\kappa d/\lambda}}$$

where

$$\begin{aligned} C &= (1+n-i\kappa)(1-n-i\kappa)(n+n_s-i\kappa)(n-n_s+i\kappa)\, e^{i4\pi nd/\lambda} \\ &\quad + (1-n+i\kappa)(1+n-i\kappa)(n-n_s-i\kappa)(n+n_s+i\kappa)\, e^{-i4\pi nd/\lambda} \end{aligned}$$

Transmittance reduces to; [30]

$$T_i = \frac{Ax}{B - Cx + Dx^2} \tag{3.87}$$

where

$$A = 16n_s\left(n^2+\kappa^2\right) \tag{3.88}$$

$$B = \left[(n+1)^2+\kappa^2\right]\left[\left(n+n_s^2\right)+\kappa^2\right] \tag{3.89}$$

$$C = \left[\left(n^2-1+\kappa^2\right)\left(n^2-n_s^2+\kappa^2\right)-4n_s\kappa^2\right]2\cos\left(4\pi nd/\lambda\right) \tag{3.90}$$

$$-\kappa^2\left[2n_s\left(n^2+\kappa^2-1\right)+2\left(n^2-n_s^2+\kappa^2\right)\right]2\sin\left(4\pi nd/\lambda\right) \tag{3.91}$$

$$D = \left[(1-n)^2+\kappa^2\right]\left[\left(n-n_s^2\right)+\kappa^2\right] \tag{3.92}$$

$$x = e^{-4\pi\kappa d/\lambda} = e^{-\alpha d} \tag{3.93}$$

Similarly, Fresnel coefficients 3.83 and 3.84 are substituted into equation 3.80

$$\begin{aligned}\mathbb{R} &= \frac{\frac{1-n-i\kappa}{1+n-i\kappa}+\frac{n-n_s-i\kappa}{n+n_s-i\kappa}e^{-i4\pi Nd/\lambda}}{1+\frac{1-n+i\kappa}{1+n-i\kappa}\frac{n-n_s-i\kappa}{n+n_s-i\kappa}e^{-i4\pi Nd/\lambda}}\\ &= \frac{(1-n+i\kappa)(n+n_s-i\kappa)+(n-n_s-i\kappa)(1+n-i\kappa)e^{-i4\pi Nd/\lambda}}{(1+n-i\kappa)(n+n_s-i\kappa)+(1-n+i\kappa)(n-n_s-i\kappa)e^{-i4\pi Nd/\lambda}}\end{aligned}$$

Then, reflectance is

$$\begin{aligned}R_i &= |\mathbb{R}|^2\\ &= \mathbb{R}\mathbb{R}^*\end{aligned}$$

$$= \frac{\left[(1-n)^2+\kappa^2\right]\left[(n+n_s)^2+\kappa^2\right]-C^+e^{-4\pi\kappa d/\lambda}+\left[(n-n_s)^2+\kappa^2\right]\left[(1+n)^2+\kappa^2\right]e^{-8\pi\kappa d/\lambda}}{\left[(1+n)^2+\kappa^2\right]\left[(n+n_s)^2+\kappa^2\right]-C^-e^{-4\pi\kappa d/\lambda}+\left[(1-n)^2+\kappa^2\right]\left[(n-n_s)^2+\kappa^2\right]e^{-8\pi\kappa d/\lambda}}$$

where

$$\begin{aligned}C^{\pm} &= \left[\left(1-n^2-\kappa^2\right)\left(n^2-n_s^2+\kappa^2\right)\pm 4n_s\kappa^2\right]2\cos\left(4\pi nd/\lambda\right)\\ &\quad +\kappa\left[2n_s\left(1-n^2-\kappa^2\right)\pm 2\left(n^2-n_s^2+\kappa^2\right)\right]2\sin\left(4\pi nd/\lambda\right)\end{aligned}$$

Reflectance then reduces to

$$R_i = \frac{E-C^+x+Gx^2}{B-C^-x+Dx^2} \tag{3.94}$$

where

$$E = \left[(1-n)^2+\kappa^2\right]\left[(n-n_s)^2+\kappa^2\right] \tag{3.95}$$

$$G = \left[(n-n_s)^2+\kappa^2\right]\left[(1+n)^2+\kappa^2\right] \tag{3.96}$$

$$B = \left[(1+n)^2+\kappa^2\right]\left[(n+n_s)^2+\kappa^2\right] \tag{3.97}$$

$$D = \left[(1-n)^2+\kappa^2\right]\left[(n-n_s)^2+\kappa^2\right] \tag{3.98}$$

$$x = e^{-4\pi\kappa d/\lambda} = e^{-\alpha d} \tag{3.99}$$

$$\tag{3.100}$$

The transmittance for a beam incident *normally* on the film from the substrate side is

$$T_i' = \frac{1}{n_s}\left|\frac{\frac{2n_s}{n_s+N}\frac{2N}{N+1}e^{-i\delta}}{1+\frac{n_s-N}{n_s+N}\frac{N-1}{N+1}e^{-i2\delta}}\right|^2 \tag{3.101}$$

$$= \frac{n_s}{1}\left|\frac{\frac{2}{n_s+N}\frac{2N}{N+1}e^{-i\delta}}{1+\frac{N-n_s}{n_s+N}\frac{1-N}{N+1}e^{-i2\delta}}\right|^2 \tag{3.102}$$

$$= \frac{n_s}{1}\left|\mathbb{T}\right|^2 \tag{3.103}$$

$$T_i' = T_i \tag{3.104}$$

If the beam enters from the substrate side, the transmittance T' is equal to T.

The Fresnel reflection coefficients for a beam incident normally on the film from the substrate side are

$$r_1' = \frac{n_s-n+i\kappa}{n_s+n-i\kappa} \tag{3.105}$$

$$r_2' = \frac{n-i\kappa-1}{n-i\kappa+1} \tag{3.106}$$

The reflected amplitude is

$$\begin{aligned}\mathbb{R}' &= \frac{\frac{n_s-n+i\kappa}{n_s+n-i\kappa}+\frac{n-1-i\kappa}{n+1-i\kappa}e^{-i4\pi Nd/\lambda}}{1+\frac{n_s-n+i\kappa}{n_s+n-i\kappa}\frac{n-i\kappa-1}{n-i\kappa+1}e^{-i4\pi Nd/\lambda}} \\ &= \frac{(n_s-n+i\kappa)(n+1-i\kappa)+(n_s+n-i\kappa)(n-1-i\kappa)e^{-i4\pi Nd/\lambda}}{(n_s+n-i\kappa)(n+1-i\kappa)+(n_s-n+i\kappa)(n-1-i\kappa)e^{-i4\pi Nd/\lambda}}\end{aligned}$$

So, the reflectance is

$$\begin{aligned}R_i' &= |\mathbb{R}|^2 \\ &= \mathbb{R}\mathbb{R}^*\end{aligned}$$

$$= \frac{\left[(n_s-n)^2+\kappa^2\right]\left[(n+1)^2+\kappa^2\right]-C^{+'}e^{-4\pi\kappa d/\lambda}+\left[(n_s+n)^2+\kappa^2\right]\left[(n-1)^2+\kappa^2\right]e^{-8\pi\kappa d/\lambda}}{\left[(n_s+n)^2+\kappa^2\right]\left[(n+1)^2+\kappa^2\right]-C^{-'}e^{-4\pi\kappa d/\lambda}+\left[(n_s-n)^2+\kappa^2\right]\left[(n-1)^2+\kappa^2\right]e^{-8\pi\kappa d/\lambda}}$$

$$\begin{aligned}C^{\pm'} &= \left[\left(n^2-n_s^2+\kappa^2\right)\left(n^2-1+\kappa^2\right)\pm 4n_s\kappa^2\right]2\cos\left(4\pi nd/\lambda\right) \\ &\quad +\kappa\left[-2\left(n^2-n_s^2+\kappa^2\right)\pm 2n_s\left(n^2-1+\kappa^2\right)\right]2\sin\left(4\pi nd/\lambda\right)\end{aligned}$$

Finally, reflectance reduces to

$$R_i' = \frac{E'-C^{+'}x+G'x^2}{B'-C^{-'}x+D'x^2} \tag{3.107}$$

where

$$E' = \left[(n_s-n)^2+\kappa^2\right]\left[(n+1)^2+\kappa^2\right] \tag{3.108}$$

$$G' = \left[(n_s+n)^2\right]\left[(n-1)^2+\kappa^2\right] \tag{3.109}$$

$$B' = \left[(n_s+n)^2\right]\left[(n+1)^2+\kappa^2\right] \tag{3.110}$$

$$D' = \left[(n_s-n)^2+\kappa^2\right]\left[(n-1)^2+\kappa^2\right] \tag{3.111}$$

$$x = e^{-4\pi\kappa d/\lambda} = e^{-\alpha d} \tag{3.112}$$

If the expressions for R_i' and R_i are compared, we see that

$$R_i' \neq R_i \tag{3.113}$$

3.6 Interaction of the Light with the Substrate Layer

There are no perfectly monochromatic sources because light has discontinuous changes in its phase. Only within a short period of time, time dependence of any light can be approximated by a sine wave. The length of this time is called the coherence time $\Delta\tau$. The coherence time can be related to the spectral bandwidth by the uncertainty principle,

$$\Delta\tau\Delta\omega \approx 2\pi \tag{3.114}$$

Equation 3.114 shows that if $\Delta\tau \to \infty$, corresponding to a wave train of infinite length, $\Delta\omega \to 0$, and a single frequency ω_o or wavelength λ_o suffices to represent the wave train. In this idealized case we have a perfectly monochromatic beam. On the other hand, as $\Delta\tau \to 0$, approximating a harmonic "spike", $\Delta\omega \to \infty$. Thus the sharper or narrower the pulse, the greater is the number of frequencies required to represent it, and so the line width, or $\Delta\lambda$, of the harmonic wave package [25]. So, the greater the coherence time, the narrower the spectral bandwidth, that is, the more monochromatic is the light [23]. The coherence length $\Delta\ell$ is the length of the traveling coherent wave and equal to

$$\Delta\ell = c\Delta\tau \approx \frac{c}{\Delta f} \tag{3.115}$$

Using $f = c/\lambda$, $\Delta\ell$ can be also written as

$$\Delta\ell = \frac{\lambda^2}{\Delta\lambda} \tag{3.116}$$

As long as the coherence length of the light satisfies the following relation [24]

$$2nd \ll \Delta\ell \ll 2n_s t \tag{3.117}$$

where t is the thickness of the substrate, incident light interacts incoherently with the substrate. This means that the character of the transmittance or reflectance spectrum is not affected by the phase changes of the wave in the substrate. The factor 2 in Equation 3.117 takes the distance traveled in the substrate or film into account and since speed of light is c/n and c/n_s in the film and substrate, respectively, n and n_s is seen in Equation 3.117.

As shown in Figure 3.5, the total transmittance and reflectance are examined where the substrate has a finite thickness t. The transmittance T_i at the film-substrate interface is reflected and transmitted at the substrate-air interface with magnitudes $T_i R_3$ and $T_i T_3$, respectively. Then the reflection beam is multiply-reflected at the substrate-film interface and is multiply-transmitted at the film-air interface. Total transmittance and reflectance can be calculated by adding all the separate partial intensities.

The transmittance is

$$\begin{aligned} T &= T_i T_3 + T_i T_3 R_3 R_i' + T_i T_3 R_3^2 R_i'^2 + T_i T_3 R_3^3 R_i'^2 + ... \\ &= T_i T_3 \left(1 + R_3 R_i' + R_3^2 R_i'^2 + R_3^3 R_i'^2 + ...\right) \\ &= \frac{T_i T_3}{1 - R_3 R_i'} \end{aligned} \tag{3.118}$$

where

$$T_3 = \frac{4n_s}{(n_s+1)^2} \tag{3.119}$$

$$R_3 = \frac{(n_s-1)^2}{(n_s+1)^2} \tag{3.120}$$

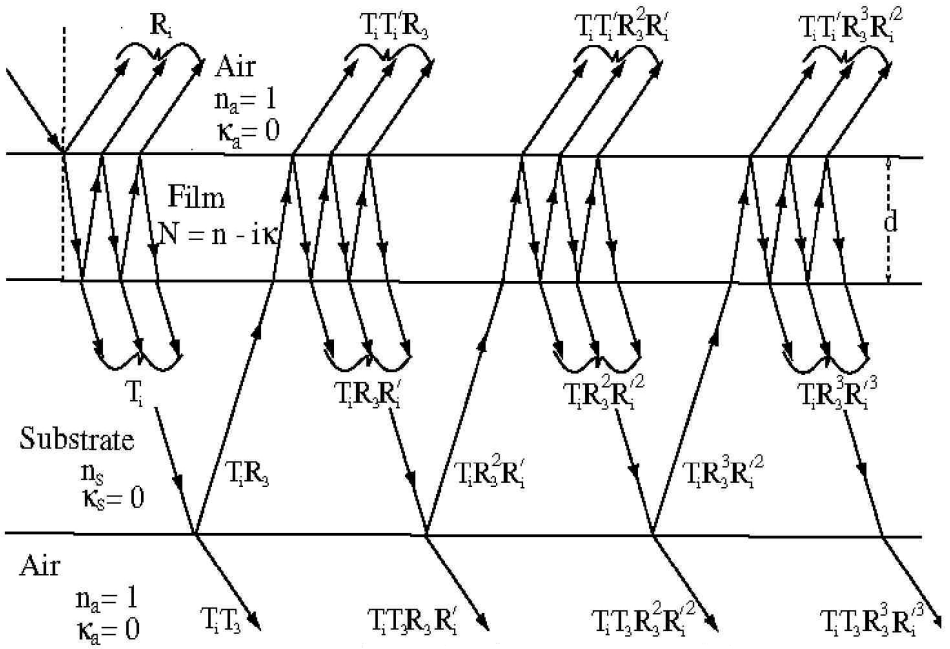

Figure 3.5: Multiply reflected and transmitted elements including the reflections at the back interface of the substrate [13]

Substituting Equations 3.87, 3.107, 3.119 and 3.120 into Equation 3.118 [19]

$$
\begin{aligned}
T &= \frac{\frac{Ax}{B-Cx+Dx^2}\frac{4n_s}{(n_s+1)^2}}{1-\frac{(n_s-1)^2}{(n_s+1)^2}\frac{E'-F'x+G'x^2}{B'-C'x+D'x^2}} \\
&= \frac{A4n_sx}{(n_s+1)^2(B-Cx+Dx^2)-(n_s-1)^2(E'-F'x+G'x^2)} \\
T &= \frac{Ax}{B-Cx+Dx^2} \qquad (3.121)
\end{aligned}
$$

where

$$A = 16n_s\left(n^2+k^2\right) \tag{3.122}$$

$$B = \left[(n+1)^2+k^2\right]\left[(n+1)\left(n+n_s^2\right)+k^2\right] \tag{3.123}$$

$$\begin{aligned} C = & \left[\left(n^2-n_s^2+k^2\right)\left(n^2-1+k^2\right)-2k^2\left(n_s^2+1\right)\right]2\cos\left(4\pi nd/\lambda\right) \\ & -\left[2\left(n^2-n_s^2+k^2\right)+\left(n_s^2+1\right)\left(n^2-1+k^2\right)\right]2k\sin\left(4\pi nd/\lambda\right) \end{aligned} \tag{3.124}$$

$$D = \left[(n-1)^2+k^2\right]\left[(n-1)\left(n-n_s^2\right)+k^2\right] \tag{3.125}$$

is obtained.

Similarly, reflectance is

$$\begin{aligned} R &= R_i + T_iT_i'R_3 + T_iT_i'R_3^2R_i' + T_iT_i'R_3^3R_i'^2 + ... \\ &= R_i + T_iT_i'R_3\left(1+R_3R_i'+R_3^2R_i'^2+...\right) \\ &= R_i + \frac{T_iT_i'R_3}{1-R_3R_i'} \\ &= R_i + \frac{T_i^2R_3}{1-R_3R_i'} \end{aligned} \tag{3.126}$$

Using Equations 3.94, 3.87, 3.107 and 3.120, reflectance becomes [20]

$$\begin{aligned} R &= \frac{E-C^+x+Gx^2}{B-C^-x+Dx^2} + \frac{\left[\frac{Ax}{B-Cx+Dx^2}\right]^2+\frac{(n_s-1)^2}{(n_s+1)^2}}{1-\frac{(n_s-1)^2}{(n_s+1)^2}\frac{E'-C^{+'}x+G'x^2}{B'-C^{-'}x+D'x^2}} \\ &= \frac{E-C^+x+Gx^2}{B-C^-x+Dx^2} + \frac{\frac{A^2x^2}{B-Cx+Dx^2}\left(n_s-1\right)^2}{\left(n_s+1\right)^2\left(B'-C^{-'}x+D'x^2\right)-\left(n_s+1\right)^2\left(E'-C^{+'}x+G'x^2\right)} \\ &= \frac{E-C^+x+Gx^2}{B-C^-x+Dx^2} + \frac{1}{B-Cx+Dx^2}\quad\frac{\mathbb{A}x^2}{\mathbb{B}-\mathbb{C}x+\mathbb{D}x^2} \end{aligned} \tag{3.127}$$

where

$$\mathbb{A} = 64n_s\left(n^2+k^2\right)^2\left(n_s-1\right)^2 \tag{3.128}$$

$$\mathbb{B} = \left[(n+1)^2+k^2\right]\left[(n+1)\left(n_s+n\right)+k^2\right] \tag{3.129}$$

$$\begin{aligned}\mathbb{C} = &\left[\left(n^2-n_s^2+k^2\right)\left(n^2-1+k^2\right)-2k^2\left(n_s^2+1\right)\right]2\cos\left(4\pi nd/\lambda\right)\\ &-\left[2\left(n^2-n_s^2+k^2\right)+\left(n^2-1+k^2\right)\left(n_s^2+1\right)\right]2k\sin\left(4\pi nd/\lambda\right)\end{aligned} \tag{3.130}$$

$$\mathbb{D} = \left[(n-1)^2+k^2\right]\left[(1-n)\left(n_s^2-n\right)+k^2\right] \tag{3.131}$$

3.7 Determination of Optical Constants of Thin Films by Transmission Spectrum

There are four unknowns in the equation of T which are n_s, n, d, and α. n_s can be calculated from the transmission spectrum of the bare substrate (See Equation 3.138);

If the multiply-reflected and transmitted beams through the substrate do not interfere, we can speak about the existence of incoherent light interaction in the substrate. This result may come out when the thickness of the substrate t is very large according to the coherence length of the light. ($t \gg \Delta\ell$). Assuming the substrate is transparent and also assuming presence of incoherent interaction in the substrate T can be calculated by summing multiply-reflected and transmitted intensities of beams as shown in Figure 3.6.

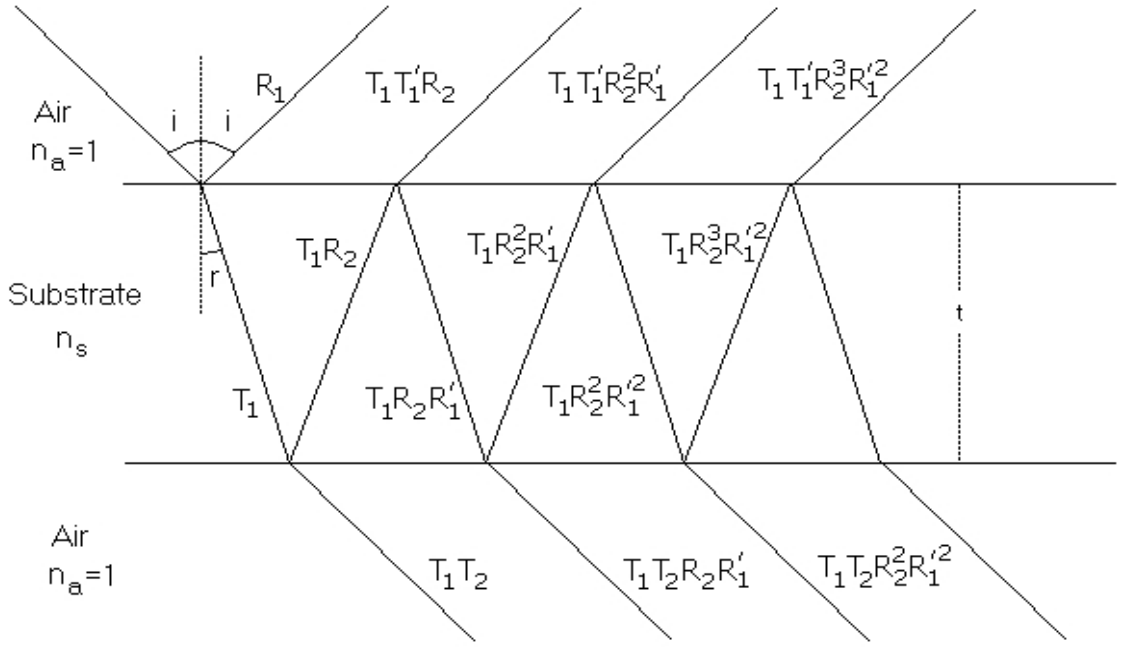

Figure 3.6: Multiple reflections and transmissions in an air-substrate-air system

$$\begin{aligned} T_s &= T_1T_2 + T_1T_2R_2R_1' + T_1T_2R_2^2R_1'^2 + ... \\ &= T_1T_2(1 + R_2R_1' + R_2^2R_1'^2 + ...) \\ &= \frac{T_1T_2}{1 - R_2R_1'} \end{aligned} \tag{3.132}$$

where

$$\begin{aligned} T_1 &= \frac{n_s}{1}\left(\frac{2}{n_s+1}\right)^2 \\ &= \frac{4n_s}{(n_s+1)^2} \end{aligned} \tag{3.133}$$

$$\begin{aligned} T_2 &= \frac{1}{n_s}\left(\frac{2n_s}{n_s+1}\right)^2 \\ &= \frac{4n_s}{(n_s+1)^2} \end{aligned} \tag{3.134}$$

$$R_1' = \left(\frac{n_s-1}{n_s+1}\right)^2 \tag{3.135}$$

Substituting intensities above into Equation 3.132, T_s becomes

$$T_s = \frac{2n_s}{n_s^2 + 1} \tag{3.136}$$

Since the substrate is transparent, reflectance R_s is

$$\begin{aligned} R_s &= 1 - Ts \\ &= \frac{(n_s - 1)^2}{n_s^2 + 1} \end{aligned} \tag{3.137}$$

Solving n_s from Equation 3.136 we have

$$n_s = \frac{1}{T_s} + \left(\frac{1}{T_s^2} - 1\right)^{1/2} \tag{3.138}$$

from where n_s can be calculated.

Equation 3.121 becomes simpler if $k = 0$. This is an acceptable approximation because k is very small over most of the transmission spectrum of the semiconductors. Then Equation 3.121 reduces to

$$T = \frac{Ax}{B - C\cos\left(\frac{4\pi nd}{\lambda}\right)x + Dx^2} \tag{3.139}$$

where

$$\begin{aligned} A &= 16n_s n^2 \\ B &= (n+1)^3(n + n_s^2) \\ C &= 2(n^2 - n_s^2)(n^2 - 1) \\ D &= (n-1)^3(n - n_s^2) \\ x &= e^{-\frac{4\pi\kappa d}{\lambda}} \end{aligned}$$

When the optical path difference is integer and half integer multiples of λ, constructive and destructive interference occurs, respectively. The equation depicting this fact is

$$2nd = m\lambda \tag{3.140}$$

where m is integer or half integer. where m=0, 0.5, 1, 1.5, ... Equation 3.140 is valid only for a dispersion-free film, however, small dispersion do not invalidate the expression [22]. Alternatively, Equation 3.140 can be expressed as

$$2nd = \left(\frac{\ell}{2} + m_1\right)\lambda \tag{3.141}$$

where m_1 is the fringe order number of the first extremum ($\ell = 0$) starting from the long wavelength. Substituting integer and half integer values of m into Equation 3.139 gives envelopes T_M for maxima and T_m for minima.

$$T_M = \frac{Ax}{B - Cx + Dx^2} \quad \text{(for maxima)} \tag{3.142}$$

$$T_m = \frac{Ax}{B + Cx + Dx^2} \quad \text{(for minima)} \tag{3.143}$$

T_M and T_m are slowly varying continuous functions of λ. These functions are the envelopes of the minima and maxima in the transmission spectrum. In the transparent region where $x = 1$, the equation for T_M reduces to

$$\begin{aligned} T_M &= \frac{2n_s}{n_s^2 + 1} \\ &= T_s \end{aligned} \tag{3.144}$$

This means, in the transparent region the envelope T_M coincides with the transmission spectrum of the bare substrate.

If the reciprocal of T_M is subtracted from the reciprocal of T_m, x can be eliminated

$$\frac{1}{T_m} - \frac{1}{T_M} = \frac{2C}{A} \tag{3.145}$$

If this equation is solved for n

$$n = \left[L + \left(L^2 - n_s^2\right)^{1/2}\right]^{1/2} \tag{3.146}$$

where

$$L = 2n_s \frac{T_M - T_m}{T_M T_m} + \frac{n_s^2 + 1}{2} = \frac{2n_s}{T_m} - \frac{n_s^2 + 1}{2} \tag{3.147}$$

For every interference fringe whether it is maximum or minimum at any λ there exists a maximum T_M for a minimum, or a minimum T_m for a maximum. The difference of the fringe order numbers of the two adjacent maxima or minima is 1.

Equation 3.140 is written for two adjacent maxima or minima as

$$2n_1 d = m\lambda_1 \tag{3.148}$$

$$2n_2 d = (m+1)\lambda_2 \tag{3.149}$$

and solving these two equations for d we find

$$d = \frac{\lambda_1 \lambda_2}{2\left(\lambda_1 n_2 - \lambda_2 n_1\right)} \tag{3.150}$$

The envelopes T_M and T_m are quadratic equations in x and can be solved for x. The solution is in the form

$$x = \frac{E - \left[E^2 - (n^2-1)^3(n^2 - n_s^4)\right]^{1/2}}{(n-1)^3(n - n_s^2)} \tag{3.151}$$

where

$$E = \frac{8n^2 n_s}{T_M} + (n^2 - 1)(n^2 - n_s^2) \quad \text{for } T_M \tag{3.152}$$

$$E = \frac{8n^2 n_s}{T_m} - (n^2 - 1)(n^2 - n_s^2) \quad \text{for } T_m \tag{3.153}$$

Since $x \ll 1$ in the strong absorption region of the spectrum, the term $\cos\left(\frac{4\pi nd}{\lambda}\right) x \sim 1$ and consequently, interference fringes can not be resolved. In this part of the spectrum, transmittance can be approximated as $T = T_o \approx Ax/B$. [19] This expression can be solved for x as

$$x = \frac{(n+1)^3(n+n_s^2)}{16n^2 n_s}$$

Similarly, envelope functions of a reflectance spectrum can be determined and calculations of optical parameters by use of envelopes can be performed as it is done for the transmittance spectrum. [20, 21] In the reflection spectrum, there is a greater number of fringes in comparison to the transmittance spectrum. Such an advantage results in reduced errors especially in d and m.

CHAPTER 4

SAMPLE PREPARATION

4.1 Substrate cleaning

It is important to use very clean materials during the deposition process. To meet this requirement, all the water was passed through deionization process before we used it. We performed the following procedure to clean silicon wafers, sliced glasses and cornings;

Firstly, all substrates were washed in deionized water with detergent, and then rinsed in running deionized water. (Rinsing process was repeated after each step during the cleaning procedure)

Secondly, they were dipped into boiling C_2HCl_3/H_2O (trichlorethylen/water) mixture with 1/1 mixing ratio, for 5 minutes. Then, the procedure followed for silicon samples were changed from that of sliced glasses and cornings.

At the third step, silicon samples were boiled in $H_2SO_4/H_2O/H_2O_2$ (sulphuric acid/water/hydrogenperoxide) mixture, having 1/2/1 mixing ratio, for about 5 minutes again. As for the glasses i.e. sliced glasses & cornings, this mixing ratio was changed to 1/10/1 and they were also boiled 5 minutes.

As a fourth step, all substrates were dipped into deionized water and agitated by ultrasound to get rid of small organic or metal particles which might reside

on them.

Finally, silicon samples were dipped into $H_2O/HCl/H_2O_2$ mixture, with mixing ratio 2/1/1, and boiled for a few minutes. On the other hand, glasses were boiled in H_2O_2 for some time, and for the last time all substrates were rinsed in deionized water.

After cleaning, substrates were dried as soon as possible by N_2 jet, and preserved in closed plastic cans.

The significance of hydrochloric acid (HCl) is that it is quite a good cleaner of metallic impurities on a surface. On the other hand sulphuric acid (H_2SO_4) is used for cleaning organic impurities on glass samples and silicon wafers.

4.2 Deposition

Various hydrogenated amorphous silicon carbide (a-$Si_{1-x}C_x$:H) films with different carbon contents were deposited at Solid State Lab, METU. Depositions were done by using PECVD system, details of which is given in the Instrumentation chapter.

In analysis, films obtained basically from four depositions were used. These depositions were named as D1, D2, D3 and D4. See Table 4.1 for the related deposition parameters.

Silicon wafers, corning glasses, and microscope cover-glasses of 1mm thickness were used as the substrates. Prior to the deposition process, transmission spectrum of the substrates (cornings and cover-glasses) at ultraviolet-visible range (300nm-1100nm) were taken by using Perkin Elmer Lambda 2s spectrometer.

Table 4.1: Parameters related to the depositions D1, D2, D3 and D4.

Deposition name	D1	D2	D3	D4
Process Pressure (torr)	0.5	0.5	0.5	0.5
Substrate Temperature (°C)	250	250	250	250
$M = C_2H_4/(C_2H_4 + SiH_4)$	0	0.2	0.5	0.7
RF Power (mW/cm^2)	90	90	90	90
SiH_4 Flow Rate(ccm)	20	16	10	6
C_2H_4 Flow Rate(ccm)	0	4	10	14
H_2 Flow Rate (with 1000ppm PH_3)(ccm)	200	200	200	200

The spectrum of cover-glass is provided on Figure 4.1 The refractive index (n_s) as a function of the wavelength (calculated using Equation 3.138 for this substrate is also shown in Figure 4.2.

Thickness measurements of the films grown on cornings and cover-glasses were done by a special thin film characterization program, Optilayer. This program uses *fitting* analysis to find the approximate thicknesses. The thicknesses of the samples found with this program are given in Table 4.2.

a-$Si_{1-x}C_x$:H films were deposited on substrates of various shapes; square, rectangle, etc. On Table 4.2, all samples are in rectangular shapes. These samples consist of rectangular substrates (microscope cover-glasses of 6 cm length) on which a-$Si_{1-x}C_x$:H films are deposited. Figure 4.3 depicts how thickness measurements are taken on such samples. Thicknesses in this table are measured in 1 cm intervals along the substrates; totally 6 measurements were done for each of those substrates. See also Figure 4.3.

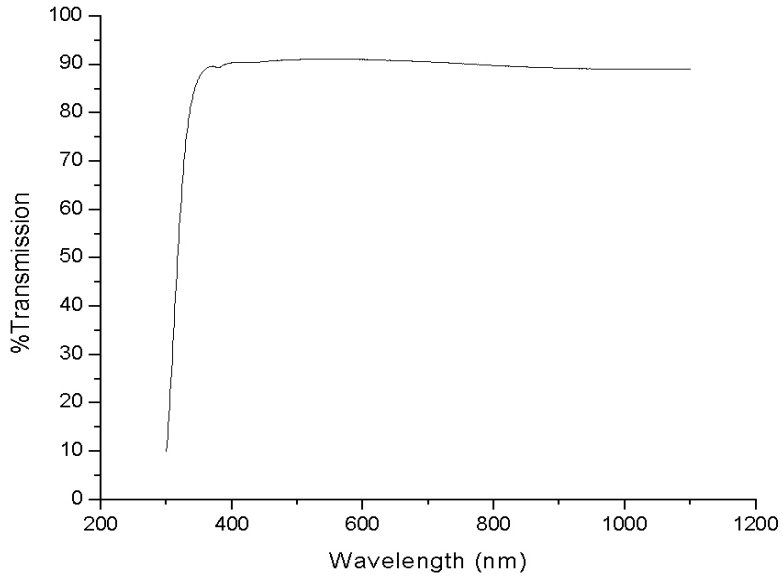

Figure 4.1: Transmission spectrum of the bare substrate (cover-glass)

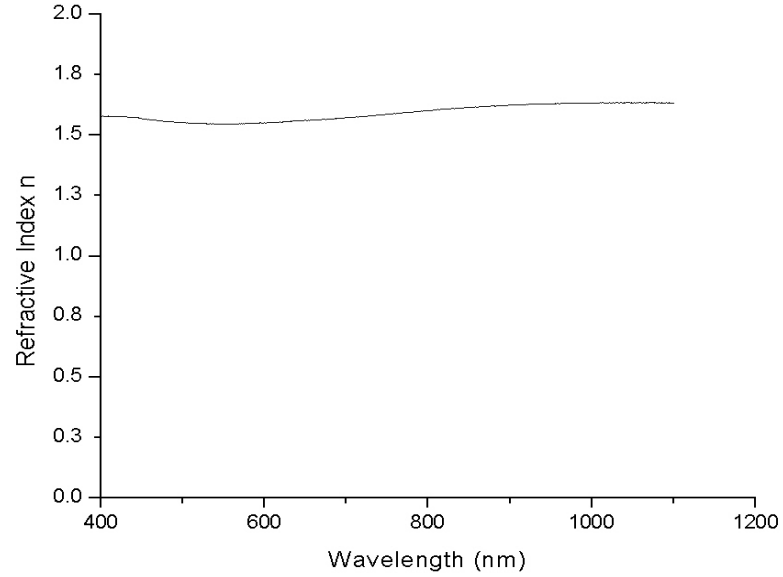

Figure 4.2: Refractive index of the bare substrate (cover-glass) changing with respect to the wavelength

Table 4.2: Film thicknesses (d) found by Optilayer program.

Sample	d_1(nm)	d_2(nm)	d_3(nm)	d_4(nm)	d_5(nm)	d_6(nm)
21c1	3267.75	1750.08	1424.26	1272.52	1079.75	1064.07
21c2	1204.39	1001	989.4	1151.26	1163.25	1193.28
21c3	3326.2	2320.52	1684.17	1563.02	1464.65	1281.67
21c4	1245.01	1572.28	1753.69	1777.98	1822.75	1263.62
24p1	535.87	541.61	610.63	688.56	945.45	1200.00
24p2	496.69	477.25	467.45	465.27	480.06	499.12
24p3	1332.84	785.16	772.46	748.3	712.38	669.7
28p1	2105.11	1609.11	1284.13	1218.61	1182.42	1142.77
28p2	1540.62	1459.18	1441.56	1439.29	1270.11	1337.08
28p3	2007.99	1830.94	1853.15	1915.2	1882.38	1882.38
28p4	1177.77	1181.13	1174.05	1171.74	1181.05	1194.41
30p1	1199.69	1238.83	1302.59	1349.42	1422.91	1731.76
30p2	1182.6	1357.46	1323.42	1121.6	1118.39	1121.76
30p3	2041.51	1679.66	1550.07	1303.55	1502.36	1493.35
30p4	1207.4	1199.68	1192.27	1185.53	1185.12	1181.32

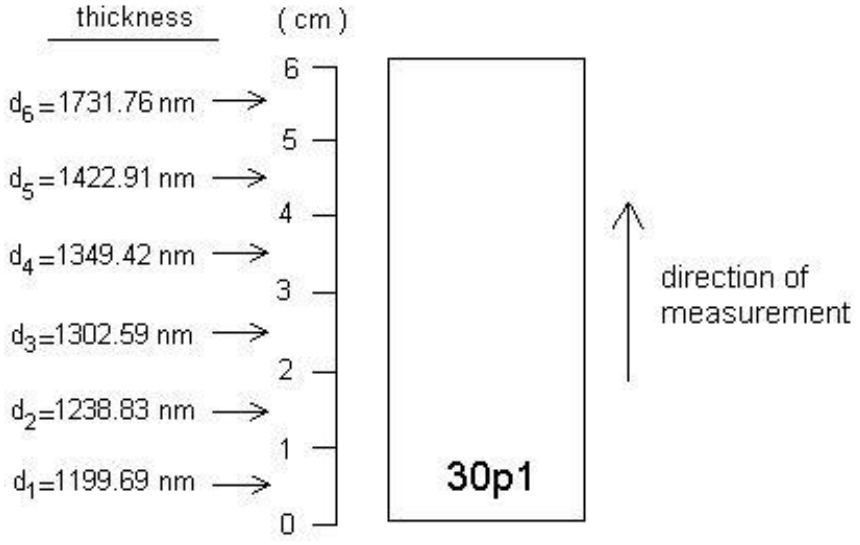

Figure 4.3: Thickness measurement of rectangular shaped substrates (microscope cover-glasses). Note that there exist a thickness variation along the substrate.

CHAPTER 5

ANALYSIS OF a-$Si_{1-x}C_x$:H FILMS IN UV-VISIBLE REGION

5.1 Transmittance Analysis of a-$Si_{1-x}C_x$:H Films

As seen in Figure 4.2, refractive index of the substrates along the transparent region (where $\alpha \approx 0$ in the range $400nm \geqslant \lambda \geqslant 1100nm$) is nearly the same. So we can take n_s as constant over a wide wavelength range. ($n_s \approx 1.59$ for cover-glass, $n_s \approx 1.53$ for corning). In Table 5.1, some of these refractive index values are given for some specific wavelengths.

Table 5.1: Values of refractive indices of the substrate (cover-glass) found from transmittance spectrum of this substrate alone. See Figure 4.2 for the integral values of n_s.

λ (nm)	1099.9	1030.9	1003.9	962.9	926.9	893.9	862.9	833.9
T_s	89.04	89.04	89.09	89.12	89.20	89.31	89.46	89.61
n_s	1.6343	1.6345	1.6325	1.6311	1.6280	1.6236	1.6173	1.6113
λ (nm)	808.9	785.9	762.9	743.9	724.9	708.9	692.9	679.9
T_s	89.75	89.95	90.14	90.24	90.42	90.53	90.59	90.71
n_s	1.6058	1.5975	1.5899	1.5857	1.5785	1.5738	1.5714	1.5664
λ (nm)	669.9	659.9	649.9	639.9	629.9	619.9	609.9	599.9
T_s	90.76	90.80	90.83	90.90	90.95	91.00	91.05	91.06
n_s	1.5646	1.5629	1.5617	1.5586	1.5566	1.5545	1.5527	1.5520

The transmission spectra of a-$Si_{1-x}C_x$:H films grown on cornings and cover-glasses have specific fringes (maxima & minima) resulted from the interference of light through the film. Figure 5.1 illustrates such fringes.

The next figure, Figure 5.2 shows the wavelength values at which local maxima and minima occur. The extremum points were obtained by utilizing *OriginPro 7.0* program. In Table 5.2, corresponding transmission values for the extrema on Figure 5.2 are given.

Table 5.2: Transmission values corresponding to extrema on Figure 5.2.

Peak type	Wavelength(nm)	$\%T$
Pos	500.9	55.72
Pos	541.9	70.85
Pos	592.9	80.20
Pos	659.9	85.19
Pos	744.9	87.28
Pos	862.9	88.02
Pos	1030.9	88.18

Peak type	Wavelength(nm)	$\%T$
Neg	514.9	52.48
Neg	562.9	61.83
Neg	622.9	67.03
Neg	698.9	69.83
Neg	800.9	71.06
Neg	940.9	71.48

Maxima and minima seen on the transmission spectrum of a-$Si_{1-x}C_x$:H films are useful when they are shown within envelopes. Figure 5.3 shows such envelopes which were obtained by interpolating (totally 200) points between maxima (for T_M's) and minima (for T_m's). In Table 5.3, T_M values with their corresponding T_m's are provided along the whole UV-Vis wavelength range. Since interpolation is limited to totally 200 points, interpolation values provided in Table 5.3 are not precise; the closest values to maxima and minima are chosen for λ_{T_m} and λ_{T_M} .

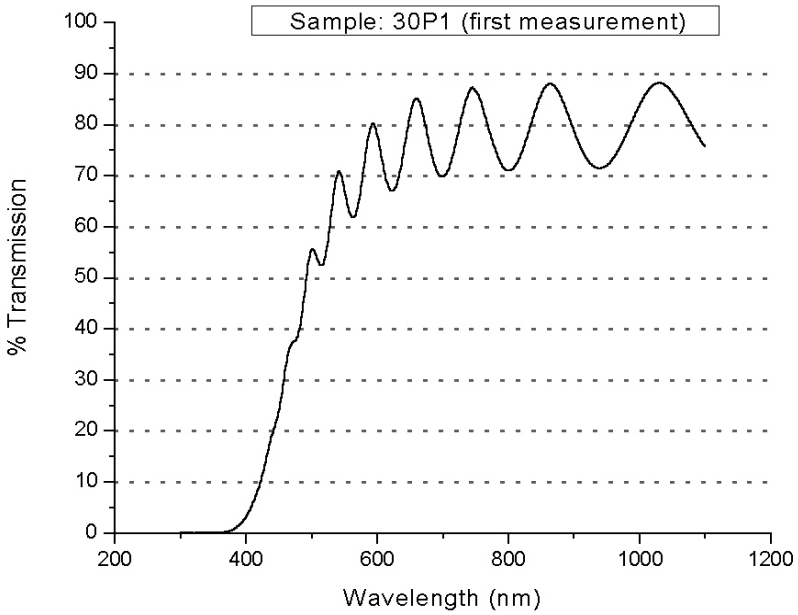

Figure 5.1: Transmission spectrum of the sample 30p1. (This is the 1st measurement within 6 measurements done for the sample 30p1).

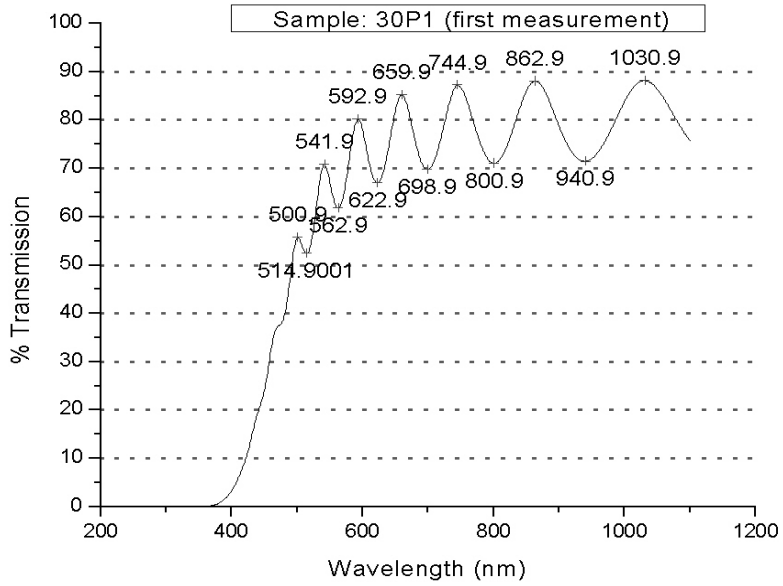

Figure 5.2: Wavelength values at which local maxima and minima occur for Figure 5.1. See Table 5.2 for the corresponding transmission values.

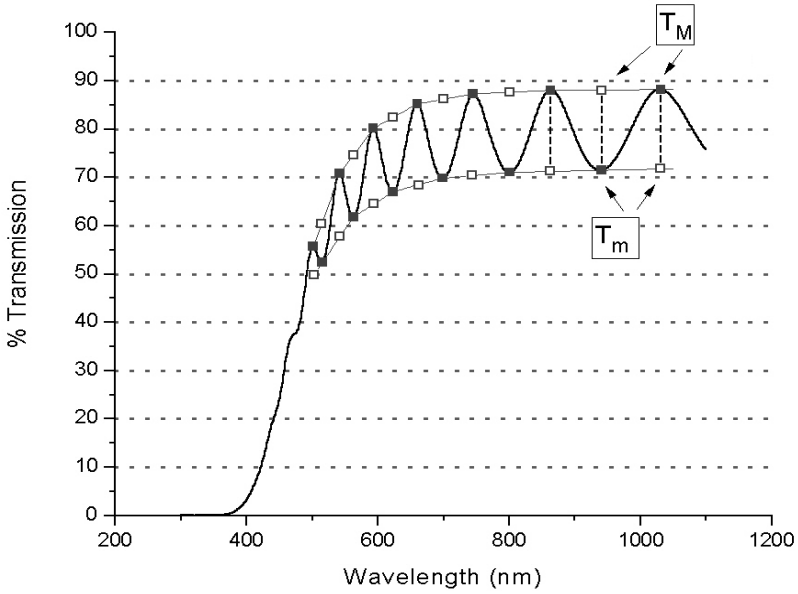

Figure 5.3: Envelopes of extrema (T_M and T_m) interpolated between maxima and minima.

5.1.1 Refractive Index (n_s) of the Bare Substrate

In ideal conditions (no thickness variation of the film, no surface inhomogeneities, no absorption) in the transparent region where $\alpha \approx 0$ (or $x \approx 1$), the substrate transmission T_s is the same as T_M (Recall Equation 3.144);

$$T_s = T_M = \frac{2n_s}{n_s^2 + 1} \tag{5.1}$$

where n_s is the refractive index of the bare substrate, and T_M is the envelope for maxima. Solving for n_s from Equation 5.1, we get

$$n_s = \frac{1}{T_M}(1 + \sqrt{1 - T_M^2}) \tag{5.2}$$

To find the approximate value of refractive index of the bare substrate from this equation, an appropriate T_M value should be chosen. Looking at Table 5.3, it

Table 5.3: Maxima (T_M) with their corresponding T_m's, minima (T_m) with their corresponding T_M's. Wavelengths of extrema (λ_{max}, λ_{min}) and interpolation values of wavelengths of extrema (λ_{T_m},λ_{T_M}) are also given.

λ_{max}(nm)	T_M	λ_{T_m}(nm)	T_m
500.9	55.72	500.00	49.58
541.9	70.85	541.46	57.65
592.9	80.20	593.97	64.52
659.9	85.19	660.30	68.40
744.9	87.28	745.98	70.39
862.9	88.02	862.06	71.24
1030.9	88.18	1030.65	71.75

λ_{min}(nm)	T_m	λ_{T_M}(nm)	T_M
514.9	52.48	513.82	60.48
562.9	61.83	563.57	74.82
622.9	67.03	624.37	82.54
698.9	69.83	698.99	86.15
800.9	71.06	801.26	87.63
940.9	71.48	942.21	88.09

is seen that the most appropriate value for T_M is 0.8818 (λ = 1030.9 nm). Using this value in Equation 5.2 gives n_s = 1.6689. Comparing this value with the n_s value for λ=1030.9 nm in Table 5.1 (n_s=1.6345) shows that the values of n_s found from T_s and from T_M do not match. The reason stems from the fact that $T_s \neq T_M$ in this case. Looking at Figure 5.4, we explicitly see that at λ=1030.9 nm, T_M and T_s values do not coincide at the same transmission value.

In such a case, one can suspect about the non-ideal conditions mentioned at the beginning of this topic. The gap between the two values may stem from a thickness variation of the film (so that the interference pattern has a irregular character along the direction of thickness variation; every transmitted element travels with a different phase angle) This effect may be reflected to the transmission spectrum of the film as *decrease in transmission values.*

Another non-ideal condition may be the absorption of the light along the film which decreases the amount of transmitted light to the other side of the film, hence decreasing the transmission values of the film from that of the substrate at

a specific wavelength.

In the first non-ideal case, a theoretical correction may help us to find the thickness variation of the film [35]. We may accept the variation of thickness homogenous in one direction, and the deviation of the thickness is considered to be symmetric with respect to the average thickness.

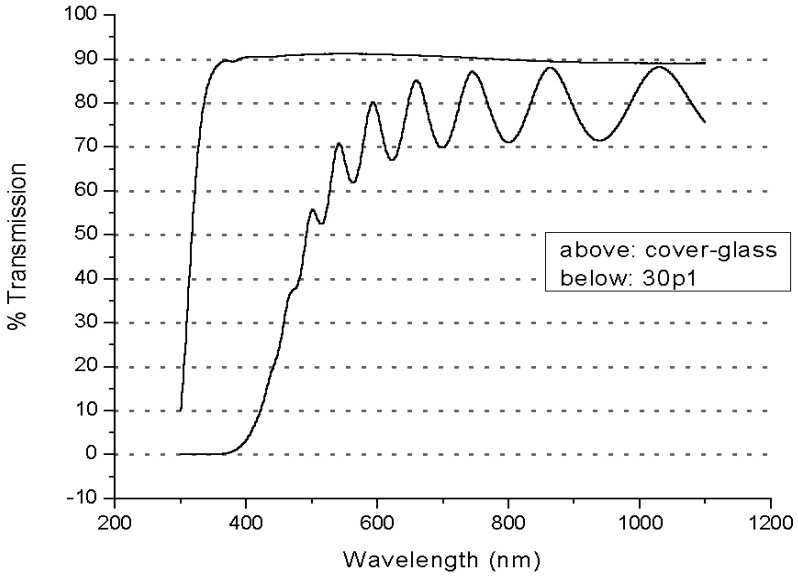

Figure 5.4: Substrate transmission T_s and transmission of the film shown together.

5.1.2 Refractive Index (n) of the Film

To calculate the approximate refractive index (n) of the a-$Si_{1-x}C_x$:H film for the sample 30p1, we need Equation 3.146, namely;

$$n = [L + (L^2 - n_s^2)^{1/2}]^{1/2} \tag{5.3}$$

where

$$L = 2n_s \frac{T_M - T_m}{T_M T_m} + \frac{n_s^2 + 1}{2} = \frac{2n_s}{T_m} - \frac{n_s^2 + 1}{2} \tag{5.4}$$

Since Equation 5.3 is valid in the transparent region ($\alpha \approx 0$), the last three T_m values in Table 5.3 may be used in Equation 5.4. These values are found as 71.75, 71.48, 71.24. Using Equations 5.3 and 5.4 (and knowing that $n_s = 1.6343$; the refractive index value for the largest wavelength) gives corresponding values for L & n seen on Table 5.4.

Table 5.4: n (refractive index of the a-SiC$_x$ film, found for the first measurement on 30p1 sample) and L values found from Equation 5.3 and Equation 5.4 respectively.

λ (nm)	T_m	L	n
1030.9	71.75	2.7201	2.2123
940.9	71.48	2.7373	2.2211
862.9	71.24	2.7527	2.2288

The average value of the three n values in Table 5.4 is 2.2207. This value can be used as the approximate refractive index of the film being analyzed.

5.1.3 Film Thickness (d)

The next step is to find the film thickness. If n_1 and n_2 are the refractive indices at two adjacent maxima (or minima) at λ_1 and λ_2 (using the basic equation for the interference fringes $2nd_1{=}n\lambda$), the equation of thickness d is constructed as (recall Equation 3.150);

$$d = \frac{\lambda_1 \lambda_2}{2(\lambda_1 n_2 - \lambda_2 n_1)} \tag{5.5}$$

While using $2nd_1=n\lambda$ we adopt that absorption is nearly zero ($\alpha \approx 0$), so that the interference fringes occur regularly under the film. Hence, in Equation 5.5, λ & n values should be taken around the region where $\alpha \approx 0$.

Looking at Table 5.2 it is seen that 862.9 nm and 1030.9 nm are the last two positive peaks (maxima) in the transmission region, so it is safe to use them to find thickness. On the other hand, in Table 5.3, T_M and T_m values can be obtained for these two wavelengths which can be used to find the corresponding refractive indices (n's) of the films at at these wavelengths (Since n value does not deviate too much, we could also take it as constant in Equation 5.5, so that $n_1 = n_2$).

The chosen values are provided in Table 5.5, where L values are found from left side of Equation 5.4 where n_s=1.6343).

Table 5.5: Values chosen to be used in Equation 5.5

λ(nm)	$\%T_M$	$\%T_m$	L	n
λ_1 =1030.9	88.18	71.75	2.69	n_1=2.1950
λ_2 =862.9	88.02	71.24	2.71	n_2=2.2072

Inserting the required parameters in Table 5.5 into Equation 5.5 gives the thickness of the film as d_1=1166.10 nm.

Note here that T_m values were found with some errors (coming from the interpolation of the envelopes). These errors lead to corresponding errors in L and n values in Table 5.5. Then, we can also consider the option of taking n as constant (n_1=n_2=2.2207 in Equation 5.5). In this case we find d_1=1192.20 nm.

Note that both of the results are close to the thickness value that we found

from *Optilayer* software (See Figure 4.3).

5.1.4 Gap Energy (E_g)

In order to evaluate the gap energy of the a-$Si_{1-x}C_x$:H film, Equation 3.71 is utilized. When this equation is rewritten in the form

$$(\alpha\hbar\omega)^2 = \hbar\omega - E_g \tag{5.6}$$

and graphed (note the linear relationship between the term $(\alpha\hbar\omega)^2$ and $\hbar\omega$), we obtain a graph such as seen in Figure 5.5.

Absorption coefficient α should be found before moving ahead. α can be found from Equation 3.151. Note here that $x = e^{-\alpha d}$;

$$x = e^{-\alpha d} = \frac{E_M - [E_M^2 - (n^2-1)^3(n^2-n_s^4)]^{1/2}}{(n-1)^3(n-n_s^2)} \tag{5.7}$$

where

$$E_M = \frac{8n^2 n_s}{T_M} + (n^2-1)(n^2-n_s^2) \qquad \text{valid for } T_M \text{ only} \tag{5.8}$$

In Equation 5.7 we need n_s, n, d and E_M to find α. We calculated n_s, n, d in this subsection before. These values are summarized in Table 5.6. In order

Table 5.6: Summary of the results, found for the first measurement of 30p1 sample. n_s is refractive index of the bare substrate, (n) is refractive index of the film coated, (d_1) is thickness of the film.

n_s	n	d_1
1.6343	2.2207	1192.20 nm

to find E_M, four T_M values are chosen near the *absorption* region. Please see

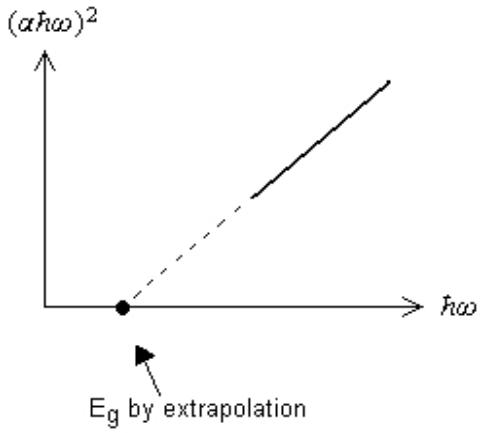

Figure 5.5: Finding the gap energy by extrapolation technique. The intercept value on x-axis gives the desired value of gap energy E_g

Figure 5.1, absorption region is approximately between 370-470 nm wavelength range where there occurs no interference fringes.

Looking at Table 5.3 we see that, desired T_M values that are used to find E_M are 55.72, 60.48, 70.85 and 74.82 for wavelentghs 500.9 nm, 514.9 nm, 541.9 nm, 562.9 nm respectively. Using these values in Equation 5.8 gives four corresponding E_M values. Each E_M value also corresponds to four α values which are found from Equation 5.7.

Finally we need the corresponding values of $(\alpha\hbar\omega)^2$ and $\hbar\omega$ (they are found in eV unit by utilizing the conversion factor $\hbar\omega(eV) = 1240/\text{wavelength}(nm)$. [18] After finding these values (by the help of values in Table 5.6), one is ready to draw a graph similar to Figure 5.5 and thus find the gap energy. The mentioned values in this paragraph are given in Table 5.7 and the resultant graph is seen on Figure 5.6.

Table 5.7: Values related to E_{gap}

Wavelength (nm)	T_M	E_M	α (cm^{-1})	$\hbar\omega$ (eV)	$(\alpha\hbar\omega)^2$ $((cm^{-1}eV)^2)$
500.9	0.5572	124.6	3557.3	2.48	77550423
514.9	0.6048	115.5	2923.6	2.41	49572398
541.9	0.7085	99.9	1713.2	2.29	15368065
562.9	0.7482	95.1	1300.5	2.20	8207325

5.2 Variations of Physical Quantities on PECVD electrode

Substrates to be deposited by a-$Si_{1-x}C_x$ films are put into places on the PECVD electrode. In order to understand how the physical parameters are affected by the distance from the center of the electrode, substrates were explicitly located at specific positions before the deposition process.

In this part of the analysis, 30p1, 30p2, 30p3, 24p1, 24p2, 24p3 samples are examined. Figure 5.7 shows the configuration of the samples 30p1, 30p2, 30p3. They were put symmetrically along the radial direction of the electrode. The same configuration is valid for 24p1, 24p2, 24p3, but not shown (they have the same shape and size as 30p's). In order to achieve some physical parameters, firstly UV-Visible spectra of the samples were obtained by Lambda 2S spectrometer. Since we deal with 30p's and 24p's, the points at which the measurements are done are depicted in Figure 5.8 to clarify the procedure. The interval between each dot is about 1 cm.

After taking the UV-Visible spectra, the spectra were analyzed with Optilayer software one by one, and some physical parameters were obtained with this software. These useful parameters are refractive indices (n), extinction coefficients

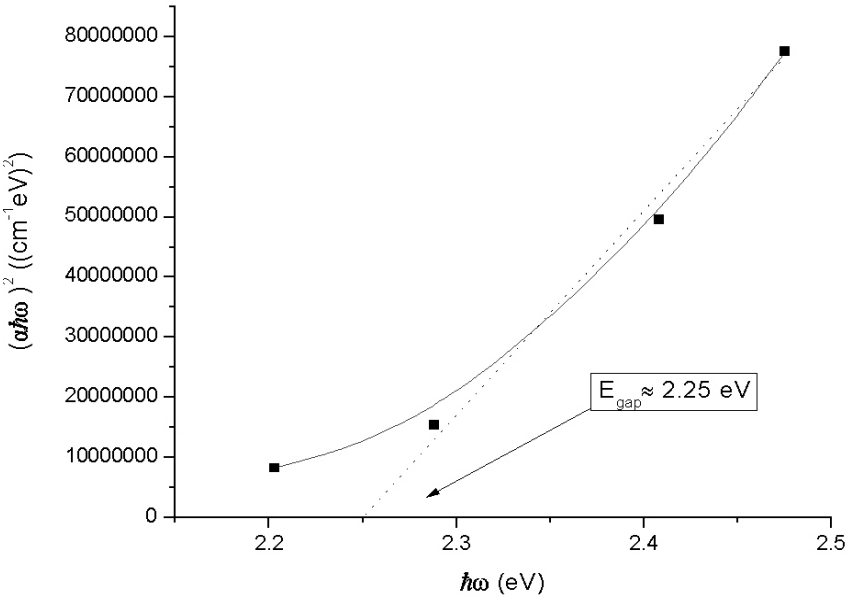

Figure 5.6: Graph of $(\alpha\hbar\omega)^2$ vs. $\hbar\omega$ values seen on Table 5.7. The dotted curve represents the extrapolation of the curve to a linear fit which crosses x-axis approximately at 2.25 eV. So, gap energy E_{gap} is approximately 2.25 eV.

(κ), and physical thicknesses of the films (d).

In the previous section it was shown that the results of Optilayer, and our analytical solutions were compatible with each other. So, it is reasonable here to use the results obtained with this software.

5.2.1 Refractive Index Behaviour Along Radial Direction on PECVD electrode

For the sake of being objective, refractive index versus wavelength graphs obtained (as the result of fitting analysis with Optilayer) are given both for 24p's and 30p's in Figure 5.10. As explicitly seen on these graphs, refractive indices

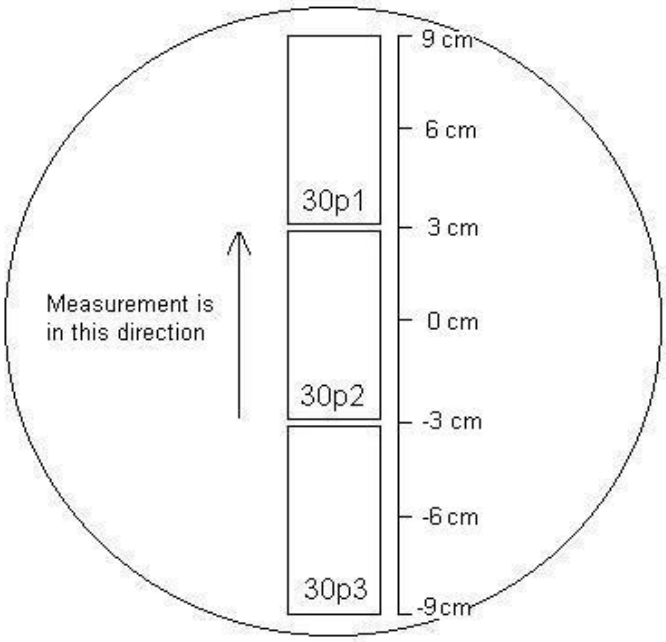

Figure 5.7: Positions of samples 30p1, 30p2, 30p3 on PECVD electrode. The same configuration is valid for 24p's.

deviate from reasonable values on the *absorption* region so values at *transmission* region (large wavelengths) are trustable. Let's, then, examine n's found at λ= 1049.1 nm. Table 5.8 gives the n values obtained at this wavelength. These values are graphed in Figure 5.9.

Table 5.8: Refractive indices at λ=1049.1 nm

Sample	n_1	n_2	n_3	n_4	n_5	n_6
24p1	3.66	3.80	3.71	3.70	3.66	3.34
24p2	3.67	3.74	3.75	3.75	3.71	3.68
24p3	3.08	3.38	3.65	3.51	3.53	3.64
30p1	2.14	2.17	2.12	2.11	2.09	2.03
30p2	2.13	2.19	2.22	2.15	2.14	2.14
30p3	1.96	2.06	2.11	2.07	2.11	2.11

As seen in Figure 5.9, there exists no selective behaviour of refractive index

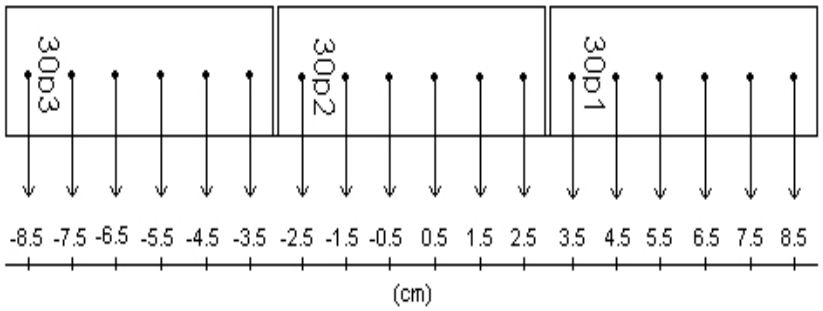

Figure 5.8: Places of measurements shown on 30p1, 30p2, 30p3 samples. Same configuration is valid for 24p's.

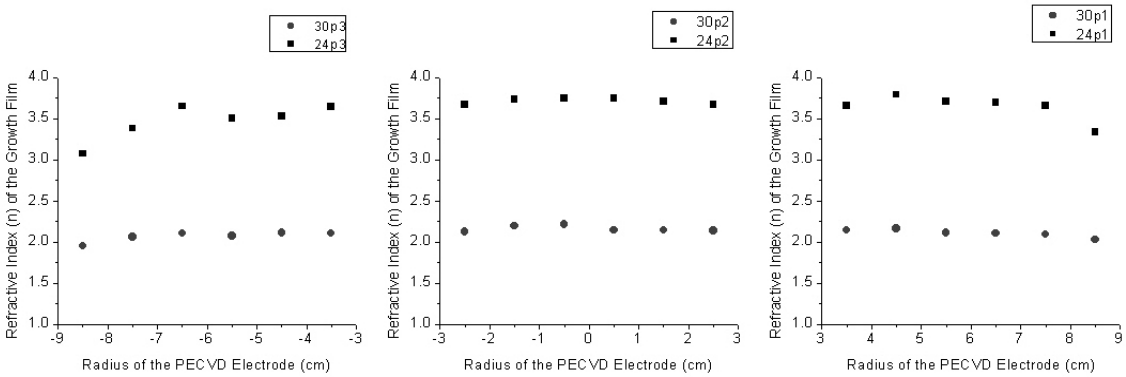

Figure 5.9: Refractive index variation along the radial direction of PECVD electrode.

n over the surface of the electrode. At the points close to the outer chamber, a little decrease is observed for both samples.

5.2.2 Film Thickness Along the Radial Direction of the Electrode

Thickness values for the same configuration seen in Figure 5.8 can be found in tabulated form on Table 4.2 for 30p's and 24p's. The graph of these values are shown in Figure 5.11. Apart from n values, thickness variation seems to have a distinguishable behaviour along the radial direction. From center to the radial

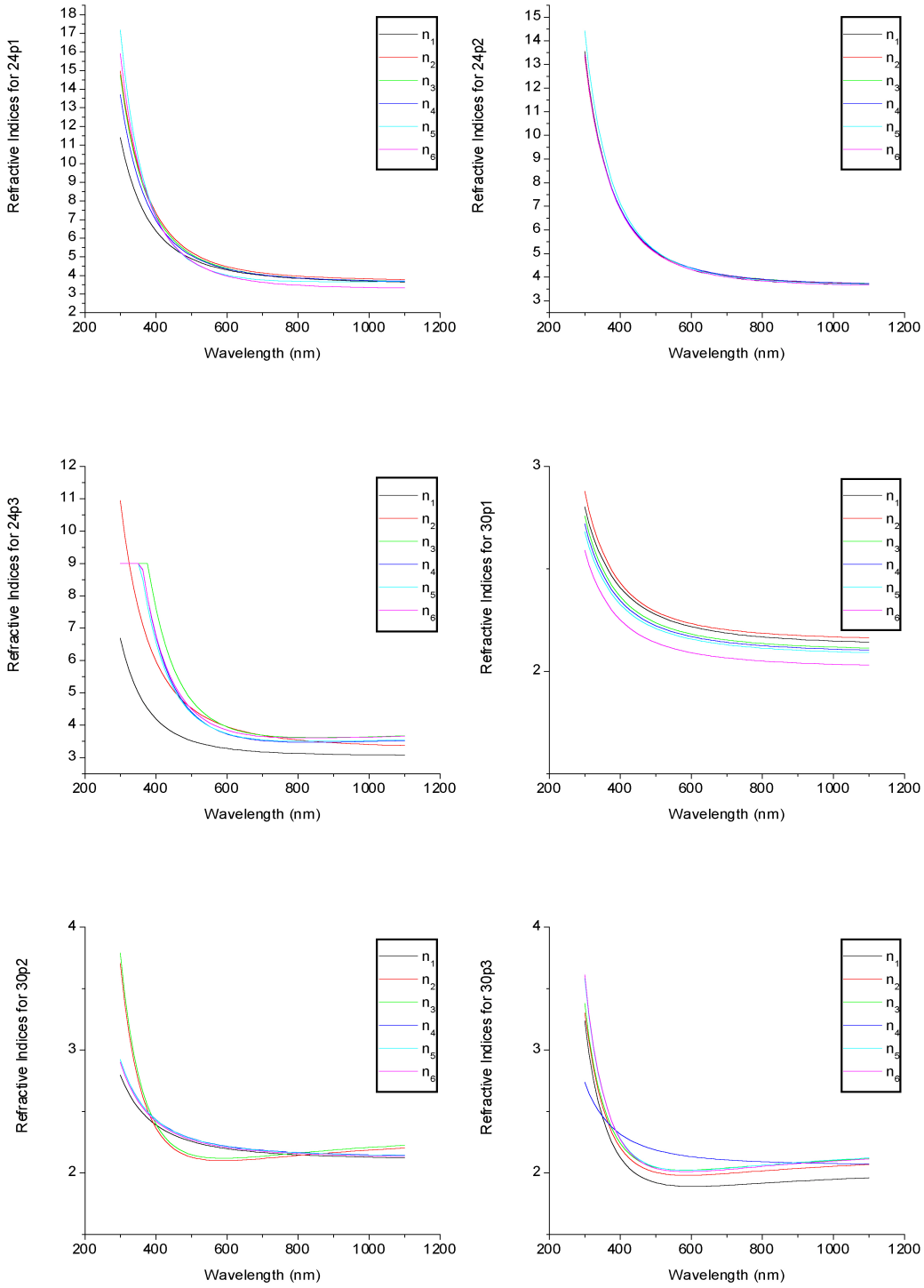

Figure 5.10: Refractive indices of samples 24p1, 24p2, 24p3, 30p1, 30p2, 30p3 with respect to UV-Vis wavelengths. Every sample has totally 6 consecutive measurements taken at 1cm intervals.

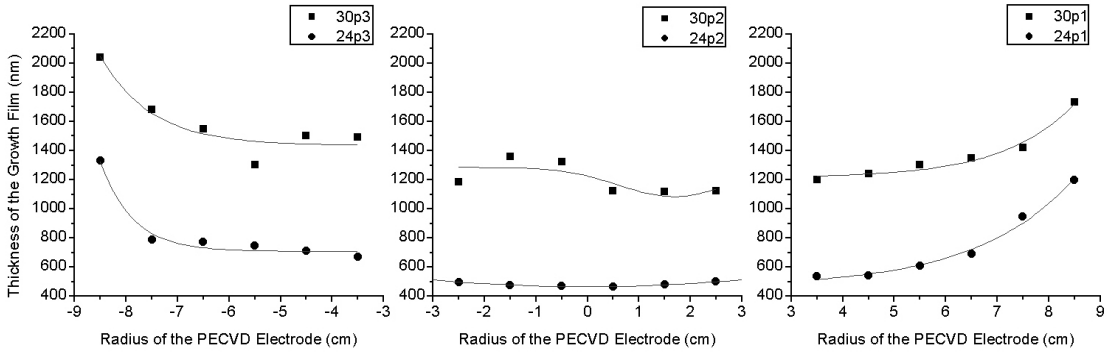

Figure 5.11: Film thickness variation along the radial direction of PECVD electrode.

direction, an increment is observed on the thicknesses of both samples (30p's and 24p's). These increments are depicted by curves in Figure 5.11. Contrary to n values, highest thickness values are observed around the rim of the electrode.

CHAPTER 6

ANALYSIS OF a-$Si_{1-x}C_x$:H FILMS IN IR REGION

In this chapter, fourier transform infrared (FT-IR) spectroscopy results will be discussed. Structural analysis of a-$Si_{1-x}C_x$:H films is performed by FT-IR transmission spectroscopy (Nicolet 520). Effect of interference due to multiple transmissions and reflectances in the thin films are eliminated by interpolating the IR absorption free regions of the spectrum. The corresponding absorption coefficient is evaluated from the simple expression of the IR transmission

$$T = e^{-\alpha d} \tag{6.1}$$

where, d is the thickness of the film.

As stated before, ethylene (C_2H_4) and silane (SiH_4) gases are used as source gases to produce a-$Si_{1-x}C_x$:H films. Relative concentration of C_2H_4 gas is defined by M=$[C_2H_4]/[C_2H_4+SiH_4]$. The main aim here is to demonstrate the effect of relative C_2H_4 concentration on infrared absorption spectra of a-$Si_{1-x}C_x$:H films.

Basically 4 samples are chosen for the analysis; S1, S2, S3 and S4, relative C_2H_4 concentrations of which are given in Table 6.1 (compatible with Table 4.1). In Figure 6.1, infrared transmission spectra of these four samples measured by Nicolet 520 FT-IR spectrometer are given along with their relative C_2H_4 concentrations depicted on them. The transmission spectra of the samples are displayed

in order to compare the features of each absorption band.

Table 6.1: Relative C_2H_4 concentrations of samples

Sample	S1	S2	S3	S4
M	0	0.2	0.5	0.7

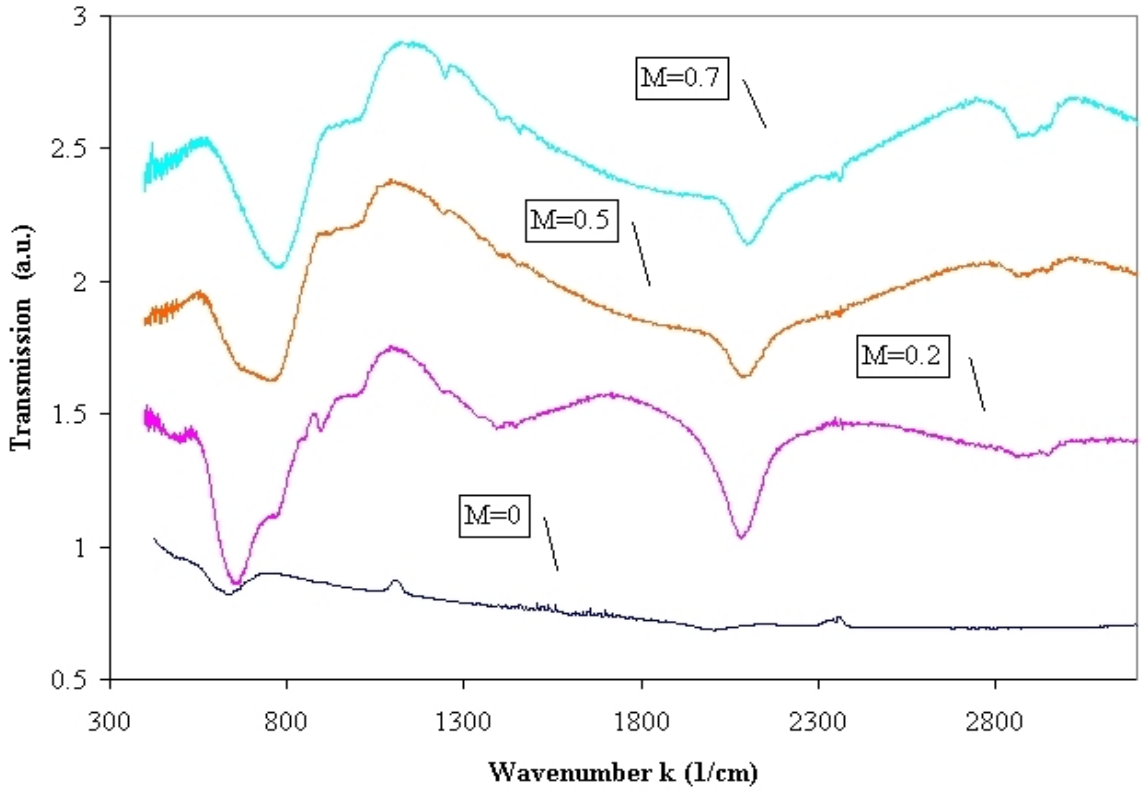

Figure 6.1: Transmission spectra of the samples

The spectra of a-$Si_{1-x}C_x$:H films shown in Figure 6.1 consists of three main absorption bands in the wavenumber ranges of 500-1500 cm^{-1}, 1900-2200 cm^{-1} and 2800-3000 cm^{-1} approximately. These absorption bands, which can also be realized from Figure 6.1 are individually shown in Figure 6.2 (a,b and c). In Figure 6.2-c no absorption peak is noticed for M=0, which means there is no

peak resulted from carbon in the range of 2700-3100 cm^{-1}. This is because of the fact that M=0 corresponds to an a-Si:H (a-$Si_{1-x}C_x$:H film with $x = 0$).

Samples S3 (M=0.5) and S4 (M=0.7) were also examined by external reflection spectroscopy (details of which are explained briefly in Sampling Techniques section) at 14° angle of incidence. The resulted spectra are compared with the transmission type spectra for the ranges 1150-1500 cm^{-1} and 2700-3100 cm^{-1} in Figures 6.3-a and Figures 6.3-b, respectively. One observes that external reflection spectroscopy provides us with enormously increased signal-to-noise ratio of the absorption spectra, which in turn enables us to identify the individual absorption peaks (found by deconvolution) more easily. So the peak frequencies are firstly found by deconvolution of the reflection spectra, and then they are used to deconvolute the actual absorption spectra measured by transmission technique.

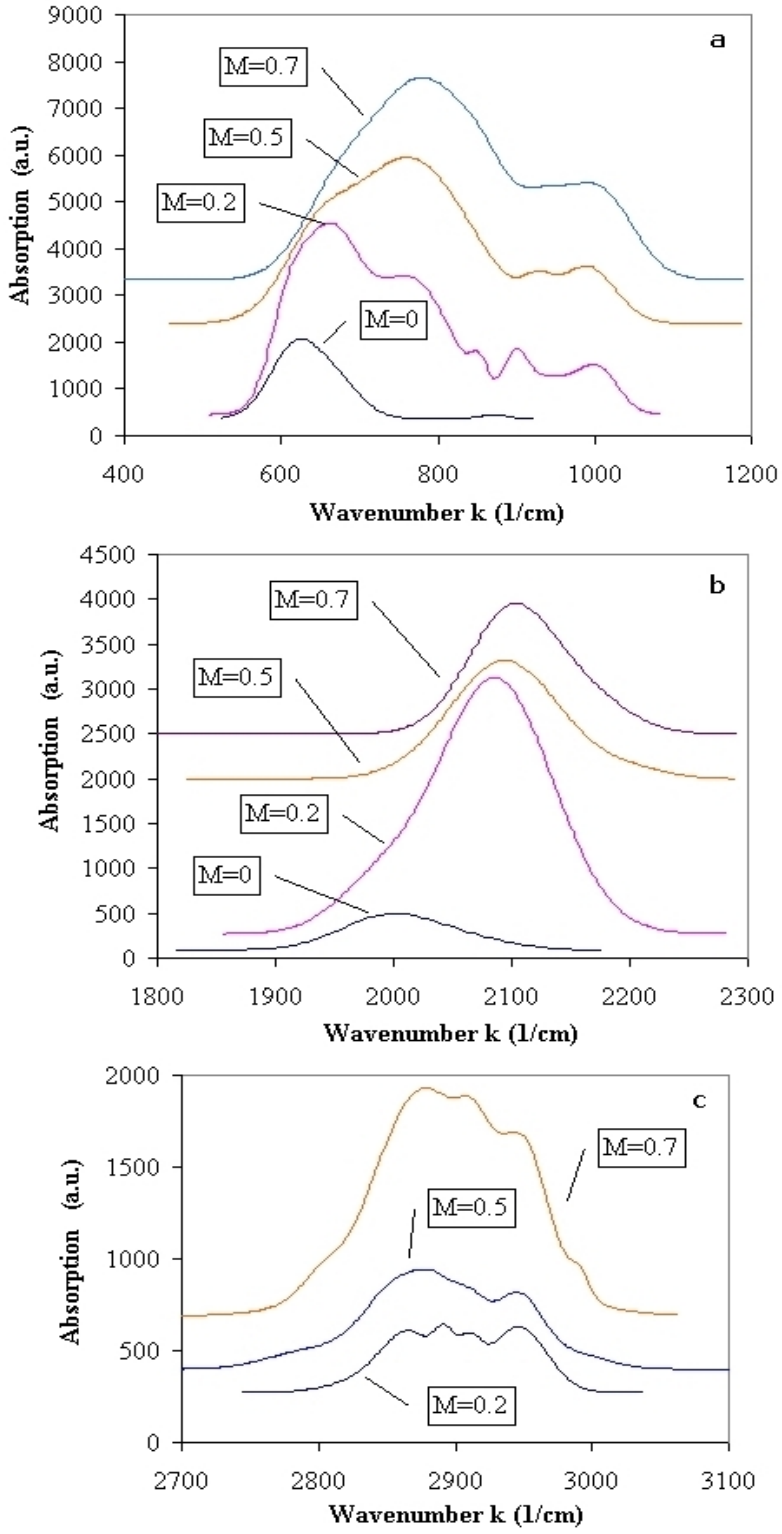

Figure 6.2: Absorption spectra found by the spectrum given in Figure 6.1 for vibrational bands around a) k=1000 cm^{-1}, b) k=2000 cm^{-1}, c) k=3000 cm^{-1}

Each absorption band consists of different vibration modes, and they are deconvoluted to find the individual peaks that constitute them. Deconvolution process is done by using a commercial software Peakfit v4.12 in light of the expected frequencies given in Table 6.2. Example of deconvoluted peaks are given (only for the sample S4) for the ranges 500-1100 cm^{-1} , 1200-1500 cm^{-1} , 1900-2200 cm^{-1} , and lastly 2700-3000 cm^{-1} in Figures 6.4-a, 6.4-b, 6.4-c and 6.4-d, respectively. Positions of the individual peaks seen on these figures are tabulated in Table 6.3 (along with their expected vibration modes determined by utilizing Table 6.2).

The bond concentrations, N, are determined by using the integrated absorption of each peak [46]

$$N = A \int \frac{\alpha(\omega)}{\omega} d\omega \tag{6.2}$$

where ω is the frequency and A is the corresponding proportionality constant.

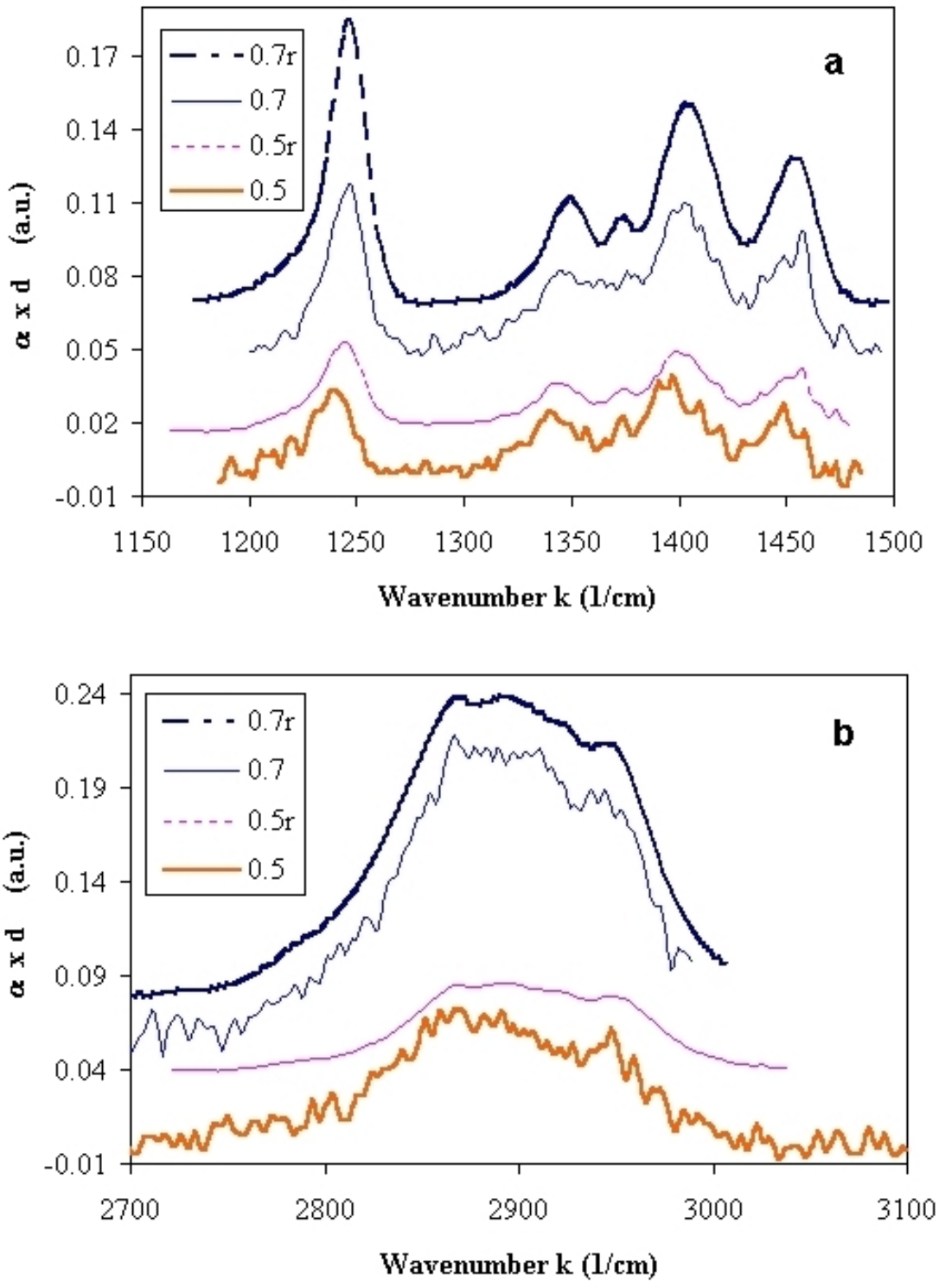

Figure 6.3: Comparison of the transmittance and reflectance (absorption) spectra of the films grown by ethylene ratio of M=0.5 and M=0.7 in the range of 1150-1500 cm^{-1} (Indices including "r" corresponds to reflectance spectra).

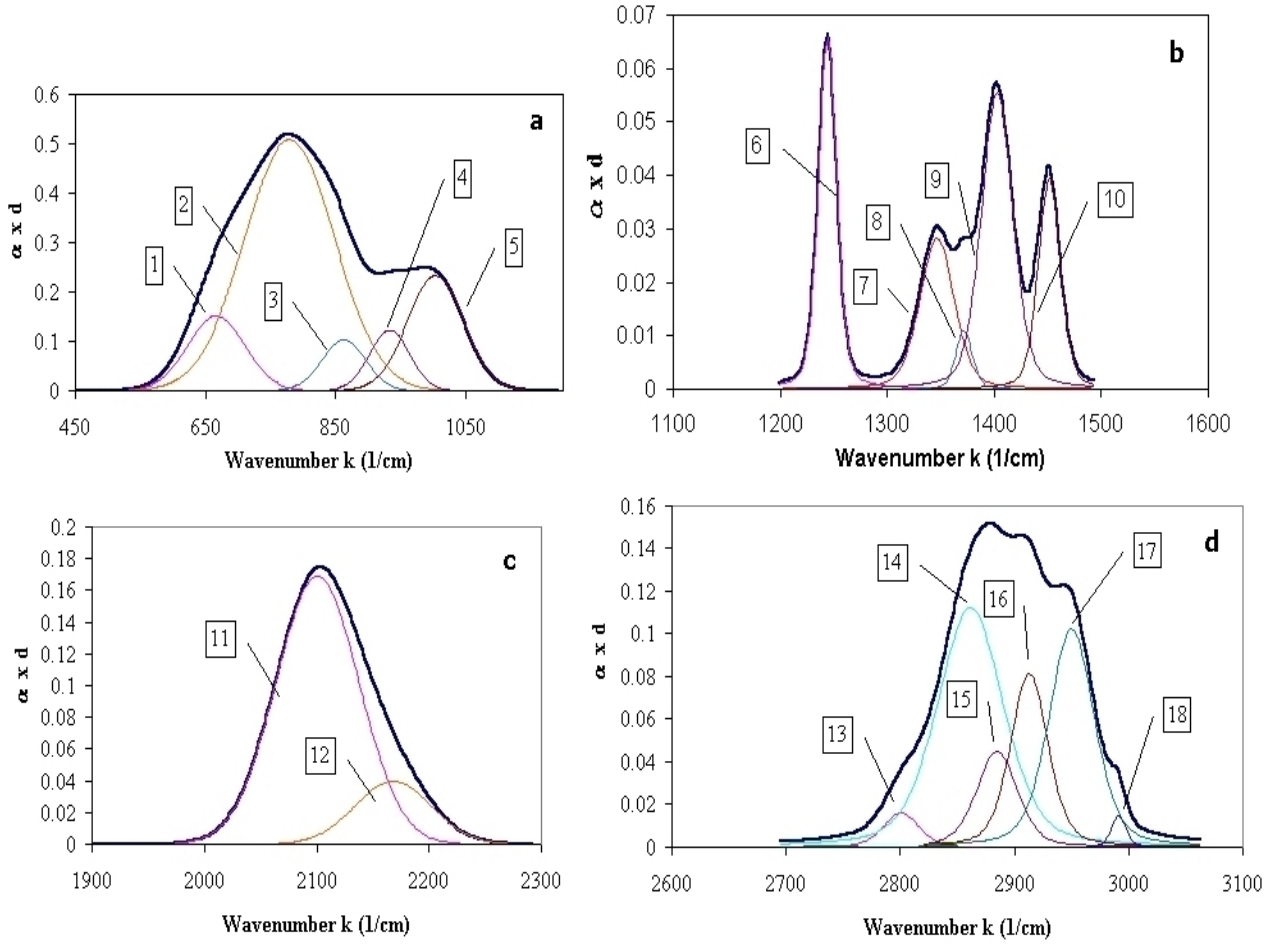

Figure 6.4: Deconvoluted absorption spectrum for sample S4, for the bands at around a) k=450-1050 cm^{-1}, b) k=1200-1500 cm^{-1}, c) k=1900-2300 cm^{-1}, d) k=2700-3100 cm^{-1}

It is clearly seen in the Figure 6.2-a that absorption peaks beyond 700 cm^{-1} start to appear as carbon is incorporated in the films. Especially, the concentration of the SiC bonds, found by using the integrated absorption of the peak P2 (at 770 cm^{-1}) and the constant A (=2.13x10^{19} cm^{-2}), is being systematically larger as M increases (shown in Figure 6.5). The wavenumber position of this peak

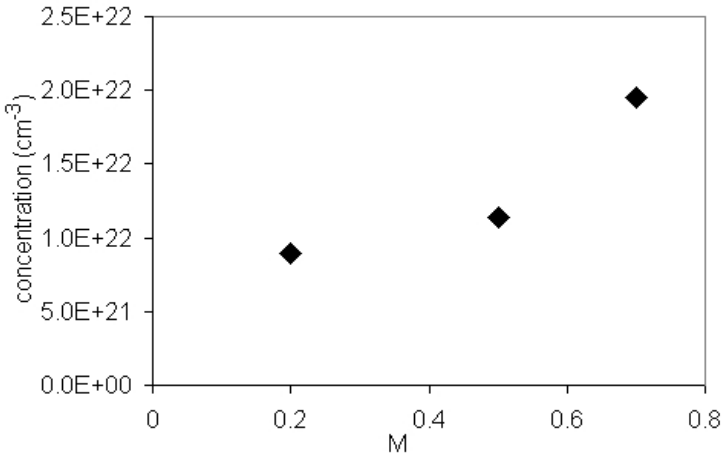

Figure 6.5: Concentration of Si-C bonds found by using the integrated absorption of the peak around 770 cm^{-1} (P2).

also slightly increases as a function of M in the range of 765-780 cm^{-1}, depicted in the Figure 6.6. These are almost in agreement with the results of Ambrosone et al. who observed that the amount of all absorption modes between 600 cm^{-1} and 1000 cm^{-1} to be increasing with C incorporation into the structure [64, 65]. As for the full width at half maximum (FWHM) value of this peak, it is found to be increasing from about 100 cm^{-1} to 150 cm^{-1} as a function of M (Figure 6.7). The FWHM is thought mainly correlated with the angular distortion of atomic

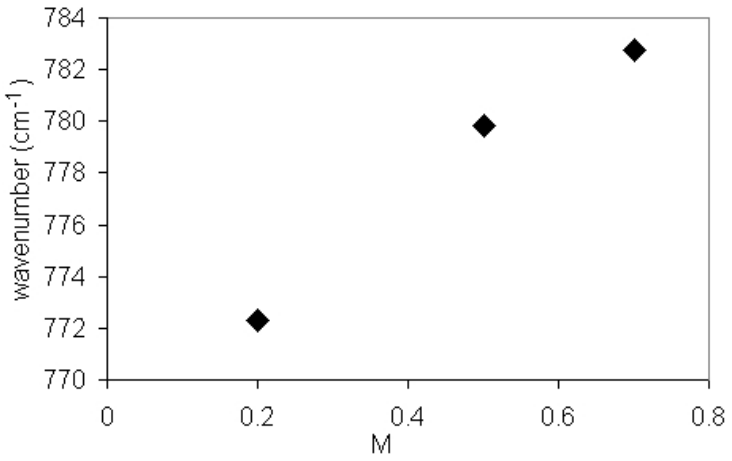

Figure 6.6: Wavenumber position of the peak around 770 cm^{-1} (P2) as a function of M

bonds. In this respect, it is reported in the literature for unhydrogenated amorphous silicon carbon alloys that angular spreads of 25° and 22° around the bond angle of 109.5° between neighboring atoms correspond to FWHM values of 245 cm^{-1} (stressed amorphous medium) and 220 cm^{-1} (relatively relaxed medium), respectively [66]. In light of this information the angular distortion of bonds in our films may be interpreted as smaller than the one in unhydrogenated a-$Si_{1-x}C_x$ thin films due to the relaxation role of hydrogen, although this distortion seems relatively increasing with carbon content x.

The concentration of Si-H wagging mode at a wavenumber of about 640 cm^{-1} reported for a-Si:H thin films abruptly decreases and tends to zero as M increases. This behaviour may misleadingly be envisaged as an elimination of Si-H bonds in the film structure if one disregards the fact that the Si-H stretching modes

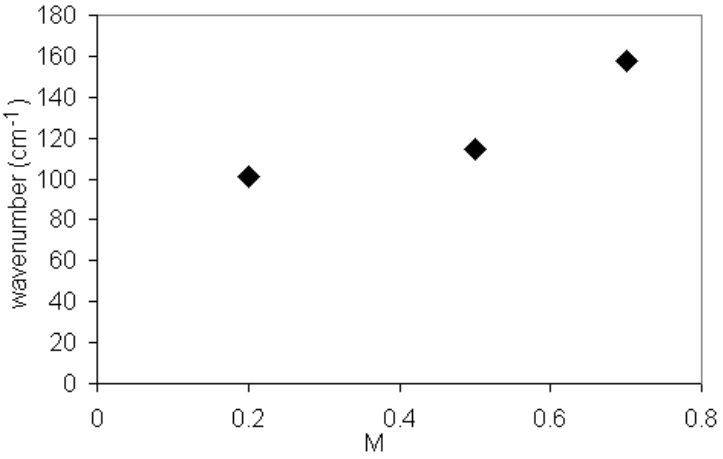

Figure 6.7: FWHM of the Si-C bond peak (located around 770 cm^{-1}).

(of wavenumbers 2000-2150 cm^{-1}) are attenuated much more smoothly as M increases. A possible explanation might be as follows for removing this controversy; The relative concentration of the peaks seen at around 670 cm^{-1} are observed to be decreasing as M increases. This composite peak might contain Si-H wagging mode whose frequency would be shifted from 640 cm^{-1} to 670 cm^{-1} (shown in the Figure 6.8) due to replacement of Si neighboring atoms with carbon atoms as their content in the films increases. For supporting this interpretation, the sum of the concentrations of these two peaks are reported as SiH bond density in Figure 6.9. Additionally, this sum reflects similar behaviour as the total concentration of Si-H_n stretching modes at about 2000-2150 cm^{-1}, as seen again in Figure 6.9. The above interpretation denies the widely adopted assignment of 670 cm^{-1} peak to the Si-C stretching mode whose concentration should have risen when x increases.

In the region between 2000-2100 cm^{-1} seen in the Figure 6.2-b (also see Figure

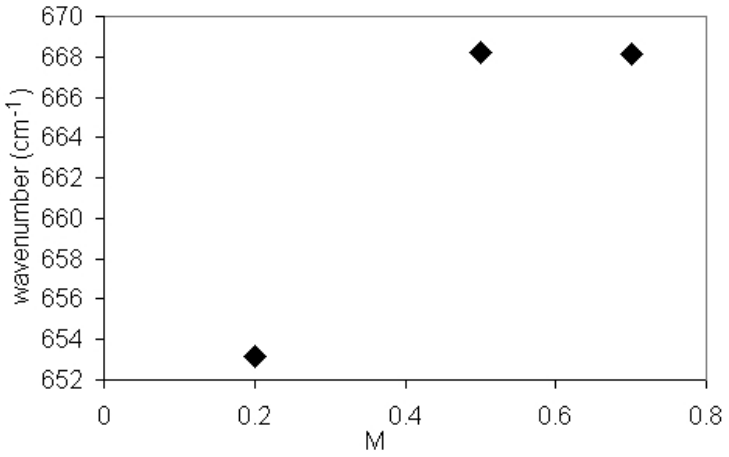

Figure 6.8: Change in frequency (wavenumber) of the bending vibration of Si-H around 640 cm^{-1}.

6.4-c), the absorption peak at 2000 cm^{-1} assigned to the Si-H stretching mode in good quality a-Si:H films disappears as carbon is incorporated in the films and replaced by a peak of substantial amount at about 2090 cm^{-1}. The replacement of Si neighbors with more electronegative carbon atoms might lead to an increase in the frequency of Si-H stretching mode from 2000 cm^{-1} towards 2070-2100 cm^{-1} depending on the number of carbon atoms bonded to Si of Si-H bond. Figure 6.10 represents a gradual shift from 2000 cm^{-1} to higher frequency of 2110 cm^{-1} as a function of carbon content [62], without any appreciable change in their FWHM values. This shift might be caused by an eventual reduction of Si-H bond length due to the higher electronegativity of carbon atom, in turn, leading to an increase in the vibration frequency of this bond. On the other hand, the concentration of this peak given in the Figure 6.11 reaches its maximum value at about M$\sim$0.2, similar to the results of Chew et al. where they found the intensity

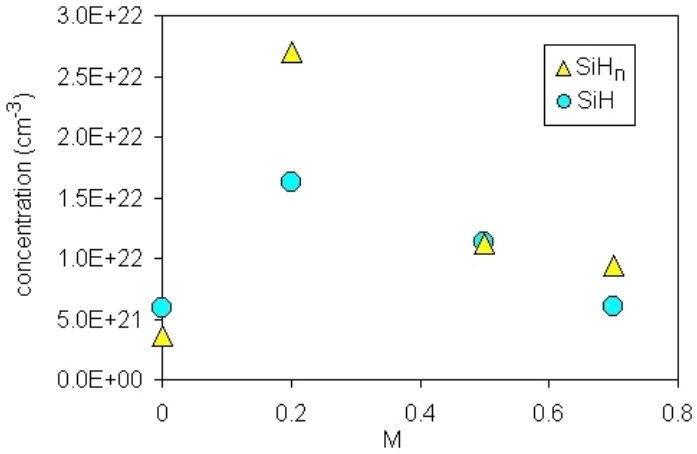

Figure 6.9: Sum of concentrations of 640 cm^{-1} and 670 cm^{-1} peaks of Si-H bonds, sum of concentrations of Si-H_n stretching modes at about 2000-2150 cm^{-1}.

of this peak is strongest at an intermediate carbon content (x$\sim$0.3). [67]. The broad absorption peak around 2150 cm^{-1} seen in the Figure 6.2-b (also see Figure 6.4-c) might correspond to similarly shifted frequency of Si-H_2 stretching mode whose original frequency is about 2090 cm^{-1} observed in the films without carbon. As a result, the whole peaks in this range might shift to higher wavenumbers as carbon is incorporated in the films and most of the hydrogen atoms might be bonded to silicon in the monohydride Si-H configuration and their concentration goes through maximum at about M$\sim$0.2; due to huge increase in the H content of the films.

The absorption band between 2800-3000 cm^{-1} shown in Figure 6.2-c is assigned to C-H_n (n=1,2 or 3) stretching vibration modes for films with $x \neq 0$. Since the frequencies of stretching modes are not mixed with other modes of vibrations, the area of peaks may reflect the density of C-H_n bonds similar to

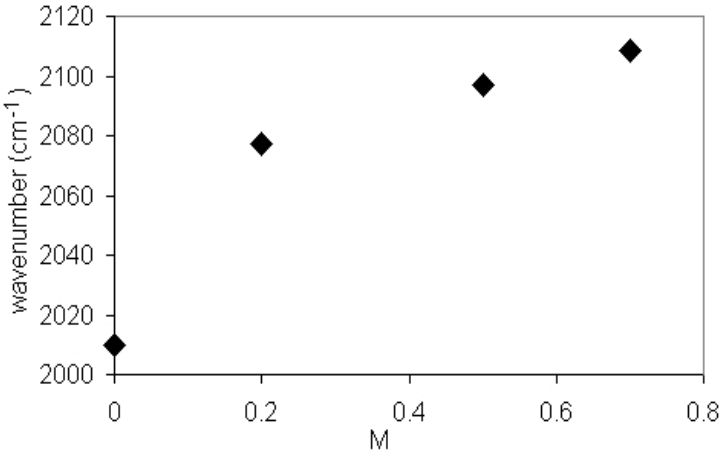

Figure 6.10: Change in the frequency of the stretching vibration of SiH_n bonds around 2000 cm^{-1}.

stretching modes of Si-H_n bonds in a-Si:H films. This band is deconvoluted into four dominant peaks (2850 cm^{-1}, 2880 cm^{-1}, 2910 cm^{-1}, 2950cm^{-1}) given in Table 6.2 (See Figure 6.4-d). The amplitudes of all the peaks increase with a small change in their frequencies and almost no change in their FWHM values as x increases. In order to see the change in concentration C-H_n (n=2,3) bonds, symmetric and asymmetric absorption peak intensities (bond densities) of each mode are added up and results are given in Figure 6.12 which carries out that concentration of both C-H_2 and C-H_3 configurations determined by using the proportionality constant, A=1.2x10^{21} cm^{-2} increases as M increases. Especially, a sharp increase in the concentration of C-H_2 is found as M changes from 0.5 to 0.7 It is also clear from this figure that the concentration of C-H_2 is observed to be always greater than that of C-H_3 except M=0.2. The overall increase in the density of CH_n bonds is also confirmed by a huge increase in the intensity of the

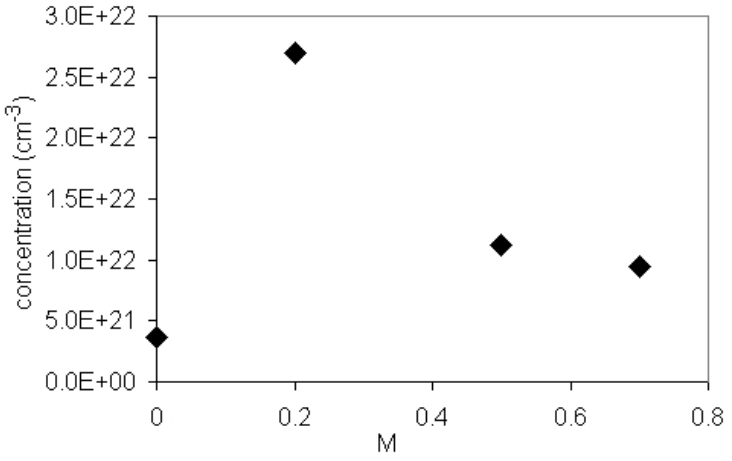

Figure 6.11: Bond concentration of the peak ($\sim$ area under the curve) around 2000-2100 cm^{-1} as a function of M.

peak around 1000 cm^{-1} as M increased from 0.5 to 0.7, clearly seen in Figure 6.13 (See also Figure 6.4-a).

The two small peaks at around 2800 cm^{-1} and 2990 cm^{-1} attributed to sp^3 type C-H bond and sp^2 type C-H_n (n=1,2) bonds, respectively, have the same character as C-H_2 and C-H_3 configurations. However, they are not considered in the analysis of relative concentrations due to their weak intensities making them difficult to distinguish from background absorption, especially for films with low carbon content. As a result, most of the hydrogen atoms bonded to carbon sites have sp^3 type C-H_2 and C-H_3 configurations.

Finally, the peak at about 3000 cm^{-1} appearing at both M=0.5 and 0.7 clearly shows that increased C ratio in the plasma promotes formation of olefinic even aromatic structures leading to sp^2 type bonds in the film structure. This behaviour is also confirmed by well distinguished peaks around 1250 cm^{-1} in Figure 6.3 for

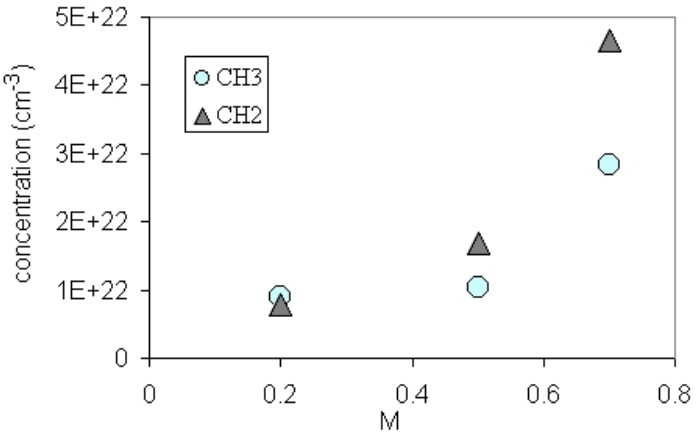

Figure 6.12: Concentrations of CH_2 and CH_3 bonds as a function of M.

the sample grown by M=0.7.

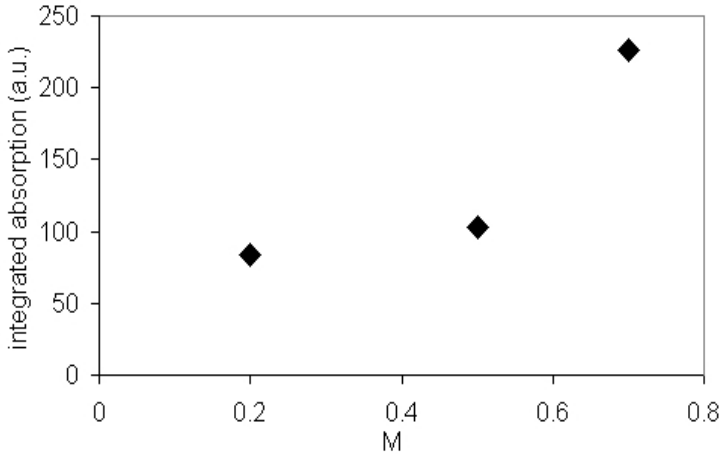

Figure 6.13: Integrated area of the peak around 1000 cm^{-1} as a function of M.

Table 6.2: Assignments of absorption peaks in FT-IR spectra of a-$Si_{1-x}C_x$:H thin films

k (cm^{-1})	Bond type and mode of vibration
640	Si-H, Wagging [47], [48, 49]
670	Si-H_n Wagging [50, 51, 52, 53, 54] Si-C Stretching [53, 54, 55, 56]
770	Si-C Stretching [47, 49, 50, 51, 57, 58, 59, 60] Si-CH_3 Rocking and/or Wagging [51, 53, 54, 56, 59, 60]
850-900	$(Si-H_2)_n$ Bending [49, 54, 61]
1000	C-H_n Wagging and/or rocking [47, 49, 50, 51, 53, 54, 58]
1245	Si-CH_3, Bending (symmetric) [47, 54, 56, 61]
1350	Si-CH_3, Bending (asymmetric) [54, 56] C-H_2 Wagging [54]
1400	C-H_2, Bending, Scissoring [54]
2000	Si-H, Stretching [49, 51, 53, 56, 61, 62]
2090 2060-2100	Si-H_2, Stretching [50, 51, 53, 61, 62] CSi-H, Stretching [50, 51, 53, 56, 61, 62]
2150	CSi-H_2, Stretching [61, 63]
2800	C-H, Stretching [49, 50, 54, 61]
2850	C-H_2, Stretching (symmetric) [47, 50, 54, 57, 60]
2880	C-H_3, Stretching (symmetric) [50, 54, 56, 57, 59, 60]
2910	C-H_2, Stretching (asymmetric) [50, 54, 56, 57, 60]
2950	C-H_3, Stretching (asymmetric) [50, 54, 56, 57, 59, 60]
2970	C-H, C-H_2, Stretching (sp^2) [60]

Table 6.3: Assignments of absorption peaks in FT-IR spectra of the sample S4 (M=0.7)

Peak No:	k (cm^{-1})	Bond type and mode of vibration
-	-	Si-H, Wagging
1	665.53	Si-H_n Wagging Si-C Stretching
2	779.34	Si-C Stretching Si-CH_3 Rocking and/or Wagging
3	862.29	$(Si\text{-}H_2)_n$ Bending
4	933.67	
5	1003.12	C-H_n Wagging and/or rocking
6	1244.25	Si-CH_3, Bending (symmetric)
7	1346.49	Si-CH_3, Bending (asymmetric) C-H_2 Wagging
8	1371.57	
9	1402.43	C-H_2, Bending, Scissoring
10	1450.66	
-	-	Si-H, Stretching
11	2100.75	Si-H_2, Stretching CSi-H, Stretching
12	2168.27	CSi-H_2, Stretching
13	2801.00	C-H, Stretching
14	2860.80	C-H_2, Stretching (symmetric)
15	2883.95	C-H_3, Stretching (symmetric)
16	2912.88	C-H_2, Stretching (asymmetric)
17	2949.53	C-H_3, Stretching (asymmetric)
18	2991.97	C-H, C-H_2, Stretching (sp2)

CHAPTER 7

CONCLUSION

Hydrogenated amorphous silicon carbide films (a-$Si_{1-x}C_x$:H) were deposited on glass and silicon substrates by the PECVD system at hand. In order to understand the effects of carbon content in film structures, depositions were done by various relative ethylene (C_2H_4) gas concentrations in plasma medium ($M=[C_2H_4]/[C_2H_4+SiH_4]$).

Throughout this work, many laboratory tools and devices (PECVD system, UV-Visible spectrometer, FT-IR spectrometer etc.) and many software (Peakfit, Optilayer, Matlab, Excel, Smartsketch, various photo-editing tools etc.) have been used and utilized starting from film deposition to data analysis.

Prior to analysis section, a theoretical background was provided to the reader at UV-Visible part. To be consistent, some results obtained by software based on numerical techniques (i.e. fitting) were compared with their analytical counterparts. These analytic results were based on this theoretical background provided beforehand.

It has been known that, real thin films deviate from homogenous, parallel-slab structure which is assumed to be the ideal model in analytical approaches. Thickness variations or surface roughness are deviations from this ideal model and

currently there are some non-ideal models developed for correcting the measured transmission spectra and hence minimizing the errors. In all analysis throughout this work, these behaviors have not been taken into consideration. Such inhomogeneity problems may be investigated in further studies as a complementary work.

Our analysis showed that there are thickness and refractive index variations on a-$Si_{1-x}C_x$:H films depending on their positions on the bottom electrode of the PECVD system. However, these were detected as slight variations around the central parts, increasing rapidly around the rim of the electrode. Samples at central positions were expected to behave ideally.

FT-IR measurements show that, in the frequency (wavenumber) range between 600-1000 cm^{-1}, integrated absorption of the peaks (hence all absorption modes in this range) increases with C incorporation in the film structure. Additionally, frequency of the peak at 770 cm^{-1} appears to increase as M increases.

It is also observed that the peak at 2000 cm^{-1} shifts to higher frequencies ($\sim$2070-2100 cm^{-1}) as C is incorporated to the film. Substantial amount of the shifted peak is concentrated at 2090 cm^{-1} (M=0.2). This shift might be caused by reduction of Si-H bond length due to higher electronegativity of the incorporated carbon atoms, leading to increase in vibrational frequency of this band.

The absorption peak around 2150 cm^{-1} seen in Figure 6.4 is thought to be the shifted frequency of Si-H_2 stretching mode whose original frequency is about 2090 cm^{-1} for films without carbon.

From the last two paragraphs it is concluded that the whole peaks in 2000-2200 cm^{-1} range shift to higher frequencies as C is incorporated in the films. Also, most of the hydrogen atoms might be bonded to silicon in monohyride Si-H configuration, concentration of which goes to a maximum at about M$\sim$0.2 due to huge increase in H content.

The absorption band between 2800-3000 cm^{-1} mainly consists of 4 dominant peaks (2850 cm^{-1}, 2880 cm^{-1}, 2910 cm^{-1}, 2950 cm^{-1}). These four peaks correspond to CH_n (n=2,3) bonds (See Table 6.3). When CH_2 and CH_3 concentrations are added within this region, it is seen that (Figure 6.12), concentrations of both CH_2 and CH_3 bonds increase as M increases (increase for CH_2 is sharper). The same increase in CH_n bonds is also seen at k$\sim$1000 cm^{-1} as M increases. (See Figures 6.2-a and 6.13). As a result, most of the H atoms bonded to C sites have (sp^3 type) CH_2 and CH_3 configurations.

REFERENCES

[1] Y. Hamakawa, Solar and Wind Technology, Vol. 7 (1989), p.235

[2] D.E. Carlson, in: Semiconductor and Semimetals, ed. by J.J. Pankove, Vol.21, Part D, 1984, p.7

[3] R.A Street, Hydrogenated Amorphous Silicon, Cambridge University Press (1991).

[4] W.G. Hawkins, D.J. Drake, N.B. Goodman, and P.J. Hartmann, Mat. Res. Soc. Symp. Proc., Vol.33, p.231 (1984)

[5] W.G. Hawkins, Mat. Res. Soc. Symp., 49, p. 443 (1985)

[6] B. Katircioglu, I. Atilgan, S. Ozder and R. Turan, Project No: TUBITAK TBAG-1538 (1998)

[7] Hydrogenated Amorphous Silicon, Part B, in: Semiconductor and Semimetals, Vol.21, ed.. by J.J. Pankove, Academic Press, New York, (1984)

[8] Physical Properties of Amorphous Materials, ed. by D. Adler, B.B. Schwartz, M.C. Steele, Plenum Press, New York, 1985.

[9] H. Tuan, Mat. Res. Soc. Symp. Proc., Vol.33, p.247 (1984)

[10] Y. Hamakawa, solar and Wind technology,7,p.235 (1989)

[11] R.C. Mc. Phedran, L.C. Botten, D.R. Mckenzie, and R.P. Netterfield, Appl. Opt., Vol.23, no. 8, p. 1197 (1984)

[12] J.C. Jans, R.W. Hollering and M. Erman, Analysis of Microelectronics Materials and Devices, ed. By M. Grasserbauer and H.W. Warner, John Wiley & Sons (1991), p.681

[13] B. Akaoglu, I. Atilgan, B. Katircioglu, Appl. Opt. Vol.39 (2000), p.1611

[14] A. A. Gulses, Ellipsometric and UV-Vis Transmittance Analysis of Amorphous Silicon Carbide Thin Films (Ph. D. Thesis, METU, 2004).

[15] W. J. Goedheer, Plasma Sources Sci. Technology, Vol.9 (2000), p.507

[16] Lambda 2 UV-VIS Spectrometer Operator‘s Manual, Bodenseewerk Perkin-Elmer GmbH, 1990

[17] Operation Manual, Univex 450 Vacuum Coating System

[18] D. Halliday, R. Resnick, J. Walker, Fundamentals of Physics 4th Edition, Appendix F p.A13 (1993)

[19] R. Swanepoel, J. Phys. E: Scientific Instruments Vol16 (1983), p.1214

[20] D.A. Minkov, J.Phys. D: Applied Physics Vol.22 (1989), p1157

[21] D.A. Minkov, J.Phys. D: Appl. Phys. Vol.22 (1989), p.199

[22] J. I. Cisneros, Appl. Opt., Vol.37 (1998) p.5262

[23] E. G. Steward, Fourier Optics: an introduction, (Halsted Press, New York, 1987)

[24] K. Lamprecht, W. Papousek, and G. Leising, Applied Optics, Vol.36 , no.25, p.6364 (1997)

[25] Frank L. Pedrotti, Leno S. Pedrotti, Introduction to Optics, Prentice Hall Int. (1993) p.253

[26] O. S. Heavens, Physics of Thin Films, ed. by G. Hass and R. E. Thun, (Academic, New York, 1964), p. 46-63

[27] J. D. Jackson, Classical Electrodynamics, (John Wiley and Sons 1975), p.281

[28] B. Akaoglu, Optical Properties of Silicon Based Amorphous Thin Films (Ph. D. Thesis, METU, 2004) p.47

[29] Frank L. Pedrotti, Leno S. Pedrotti, Introduction to Optics, Prentice Hall Int. (1993) p.419

[30] J. C. Manifacier, J. Gasiot, and J. P. Fillard, Journal of Physics E : Scientific Instruments, Vol.9, p.1002 (1976)

[31] I. Atilgan, The Production and Characterization of Si Thin Films (Ph. D. Thesis, METU, 1993). p.112-125

[32] K. Sel, The Production of Light Emitting PIN Diodes Based on the Plasma Deposited Amorphous Silicon Carbide Films, (MS Thesis, METU, 2002)

[33] O. Ozdemir, Instability Studies in Amorphous Silicon Based Alloys, (Ph. D. Thesis, METU, 2004) p.51-54

[34] H. Conrads, M. Schmidt, Plasma Sources Sci. Technology, Vol.9 (2000) p.441

[35] B. Akaoglu, Determination of Optical Costants of Silicon Based Amorphous Films by UV-Visible Transmittance and Reflectance Measurements, (M.S. Thesis, METU, 1998) p.31-35

[36] S. Gasiorowicz, Quantum Physics, (John Wiley and Sons, 1974), p.342

[37] J.J. Sakurai, Modern Quantum Mechanics, (Addison Wesley Publishing, 1994), p.337

[38] F. Bassani, Optical Properties of Semiconductors, ed. by G. Martinez, (Kluwer Academic Publishers, 1993), p.40

[39] J.J. Sakurai, Modern Quantum Mechanics, ed. by S.F. Tuan, (Addison-Wesley Publishing, 1994), p.336

[40] M. Jaros, Deep Levels in Semiconductors, (Adam Hilger Ltd, Bristol, 1982), p.148

[41] K.W. Böer, Survey of Semiconductor Physics: Electrons and Other Particles in Bulk Semiconductors, (Van Nostrand Reinhold, 1990), p.334

[42] K.W. Böer, Survey of Semiconductor Physics: Electrons and Other Particles in Bulk Semiconductors, (Van Nostrand Reinhold, 1990), p.336

[43] J.R.Reitz, J. Milford, R.W.Christy, Foundations of Electromagnetic Theory, (Addison-Wesley Publishing, 1992), p.403

[44] J.R.Reitz, J. Milford, R.W.Christy, Foundations of Electromagnetic Theory, (Addison-Wesley Publishing, 1992), p.410

[45] Nicolet FT-IR 520 Spectrometer User‘s Manual

[46] F. Giorgis, F.Giuliani, C.F.Pirri, V. Rigato, E.Tresso and S.Zandolin, Properties of Amorphous Silicon and its Alloys, ed. by Tim Searle (INSPEC, London, 1998), pp.74-78.

[47] I. Ferreira, M. E. V. Costa, L. Pereira, E. Fortunato, R. Martins, A. R. Ramos, M. F. Silva, Appl. Surf. Sci., Vol.184 (2000), p.8

[48] Y. Catherine, A. Zamouche, J. Bullot, M. Gauthier, Thin Solid Films, Vol.109 (1983), p.145

[49] P.I. Rovira, F. Alvarez, Phys. Rev. B, Vol.55 (1997), p.4426

[50] Y. Katayama, K. Usami, T. Shimada, Philos. Mag. B, Vol.43 (1981), p.283

[51] F. Demichelis, C.F. Pirri, E. Tresso, T. Stapinski, J. Appl. Phys., Vol.71 (1992), p.5641

[52] D. R. McKenzie, J. Phys. D:Appl. Phys., Vol.18 (1985), p.1935

[53] R.A. C. M. M. van Swaaij, A.J.M. Berntsen, W.G.J.H.M. van Sark, H. Herremans, J. Bezemer, W.F. van der Weg, J. Appl. Phys., Vol.76 (1994), p.251

[54] J. Bullot, M.P. Schmidt, Phys. Stat. Sol. (b), Vol.143 (1987), p.345

[55] H. Herremans, Grevendonk, R.A. C. M. M. van Swaaij, W.G.J.H.M. van Sark, A.J.M. Berntsen, W.M. Arnold Bik, J. Bezemer, Philos. Mag. B, Vol.66 (1992), p.787

[56] H. Weider, M. Cardona, C.R. Guarnieri, Phys. Stat. Solid. B., Vol.62 (1979), p.99

[57] Y.M. Li, B.E. Fieselmann, Appl. Phys Lett., Vol.59 (1991), p.1720

[58] G. Leo, G. Galluzzi, G. Guattari, R. Viicenzoni, F. Demichelis, G. Ciovini, C.F. Pirri, E. Tresso, J. Non.Cryt. Solids, Vol.164-166 (1993), p.1035

[59] S. Lin, S. T. Chang, J. Phys. Chem. Solids, Vol.59 (1998), p.1399

[60] F. Demichelis, F. Giorgis, C.F. Pirri, E. Tresso, Phil. Mag. A, Vol.72 (1995), p.913

[61] Y. Tawada, K. Tsuge, M. Condo, H. Okamoto, Y. Hamakawata, J. Appl. Phys., Vol.53 (1982), p.5273

[62] G. Lucovsky, Solid State Communications, Vol.29 (1979), p.571

[63] B.K. Agrawal, J. Non-Cryst. Solids, Vol.114 (1989), p.519

[64] G. Ambrosone, P. Capezzuto, S. Catalanotti, U. Coscia, S. Mormone, Philosophical Magazine B, Vol.80 (2000), p.497

[65] G. Ambrosone, V. Ballarini, U. Coscia, S. Ferrero, F. Giorgis, P. Maddalena, A. Patelli, P. Rava, V. Rigato, Thin Solid Films, Vol.427 (2003), p. 279.

[66] G. Foti, Appl. Surf. Sci., Vol.184 (2001), p. 20.

[67] K. Chew, Rusli, S.F. Yoon, V. Ligatchev, E. J. Teo, T. Osipowicz, F. Watt, J. Appl. Phys., Vol.92 (2002), p.2937

[68] B. Racine, A.C. Ferrari, N.A.Morrison, I. Hutchings, W.I. Milne, J. Robertson, J. Appl. Phys., Vol.90 (2001), p.5002